國立臺灣大學工學院化學工程學系

碩士論文

Department of Chemical Engineering

College of Engineering

National Taiwan University

Master's Thesis

以分子動力學模擬探討甲硫胺酸對二氧化碳水合物生長及成核的促進效果

Investigation of the Promotional Effects of Methionine on the Growth and Nucleation of Carbon Dioxide Hydrates via Molecular Dynamics Simulation

劉俊杰

Chun-Chieh Liu

指導教授：林祥泰 博士

Advisor: Shiang-Tai Lin, Ph.D.

中華民國 113 年 7 月

July 2024

doi:10.6342/NTU202403841

致謝

在碩班的這兩年中我邂逅了許多的人事物，即便不一定所有事都是完全順遂的，但最後我仍順利的完成論文並拿到學位，我認為有太多的人必須感謝了。首先是我的指導教授林祥泰老師，在初期我對研究內容還不甚了解時，他願意不厭其煩地向我解釋各種研究相關的知識，並時常和我分享一些新穎的輔助工具讓我在研究上能更快得心應手，在後期研究過程中遇到瓶頸時，祥泰老師總是能提供我一些解決問題的新思路，並一步步引導我得到更好的結果，讓我能在研究方面不斷前行，實在是感激不盡。再來是實驗室的成員們，感謝晨軒在實驗室管理及維護方面的諸多貢獻，讓我們能安心的做研究。感謝亮堯提供我許多研究方面的建議並解答了不少我在研究上遇到的問題，你是水合物組的最大支柱。感謝彥任、興豪在實驗室環安衛及各種活動日程安排等工作上的協助。感謝前一屆的肇廷、子新、庭嘉、峻承當時給予我們這些新生的許多建議，讓我能更快適應碩班生活。感謝同屆的岳和力曦時常和我分享一些生活上的趣事和研究上的進展，讓我的碩班生活不無聊。感謝晙維、晉安、翔云的加入，活躍了實驗室的氣氛。感謝 Dalip 和 Sanchari 讓我時常有練習英文口說及聽力的機會。

最後，我要感謝我的父母、姊姊和弟弟，感謝我的家人們對我的支持，讓我能無後顧之憂的順利過完碩班生涯。

doi:10.6342/NTU202403841

中文摘要

由於甲硫胺酸已被許多研究證實為二氧化碳水合物的促進劑，但目前仍尚未有研究結果表明其促進機制，因此本研究的目的是透過分子動力學（MD）模擬來探討甲硫胺酸對二氧化碳水合物成核和成長過程的影響，並進一步找出其促進機制。我們的模擬包含二氧化碳水合物的成核以及成長兩個部分，關於二氧化碳水合物的成長，從模擬結果可以看出當初始系統的液相中存在低濃度(0.56 wt%)的甲硫胺酸時對二氧化碳水合物的生長過程會有促進效果，而目前有發現甲硫胺酸具有促進效果的研究中所使用的甲硫胺酸濃度也都在 1.0 wt%以下，因此我們的模擬結果和實驗結果相當一致。另外，我們觀察到當在模擬過程中甲硫胺酸存在於水合物和液體的界面附近的數量較少時，才能觀察到對二氧化碳水合物的生長的促進效果，同時我們也發現添加甲硫胺酸會增加二氧化碳分子的擴散係數，加快其質傳速率，這應為甲硫胺酸主要的促進原因。

而對於二氧化碳水合物的成核，在我們模擬的溫度和壓力條件下，並未觀察到甲硫胺酸對水合物成核速率有具有統計學意義的促進效果，然而我們發現在壓力為 30 bar 且過冷溫度約為 26 K 時，初始液相中含有 0.82 wt%甲硫胺酸的系統在成核後水合物的生長速率相較於無添加甲硫胺酸的系統約有 36.61%的提升，此濃度和先前二氧化碳水合物生長測試中觀察到的促進現象的甲硫胺酸濃度(0.56 wt%)相當接近，再次表現出了結果的一致性。經過分析後得知，在水合物生長過程中有

doi:10.6342/NTU202403841

甲硫胺酸靠近的那一側水合物會生長的較快，顯示出甲硫胺酸對於二氧化碳水合物生長的潛在貢獻。

關鍵字:

分子動力學模擬、二氧化碳水合物、胺基酸、甲硫胺酸、動力學水合物促進劑

doi:10.6342/NTU202403841

ABSTRACT

Due to the fact that methionine has been confirmed by many studies as a promoter of CO_2 hydrate formation, but the mechanism of this promotion has not yet been clarified, the purpose of this study is to investigate the effect of methionine on the nucleation and growth processes of CO_2 hydrate through molecular dynamics (MD) simulations and to further identify its promoting mechanism. Our simulations include both the nucleation and growth of CO_2 hydrate. Regarding CO_2 hydrate growth, the simulation results show that the presence of low concentrations (0.56 wt%) of methionine in the initial liquid phase of the system promotes the growth of CO_2 hydrate. The concentrations of methionine found to have a promoting effect in previous studies are also below 1.0 wt%, indicating a high degree of consistency between our simulation results and experimental findings. Additionally, we observed that the promotion of CO_2 hydrate growth is evident when a smaller amount of methionine molecules is present near the hydrate-liquid interface during the simulation process. We also found that the addition of methionine increases the diffusion coefficient of CO_2 molecules, accelerating their mass transfer rate, which is likely the main reason for methionine's promoting effect.

For the nucleation of CO_2 hydrate, our simulations did not show a statistically significant promoting effect of methionine on the nucleation rate under the temperature

doi:10.6342/NTU202403841

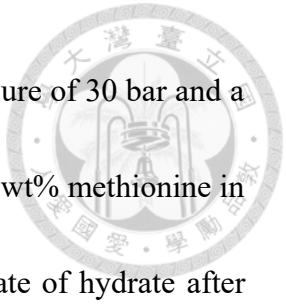

and pressure conditions simulated. However, we found that at a pressure of 30 bar and a subcooling temperature of approximately 26 K, the system with 0.82 wt% methionine in the initial liquid phase exhibited a 36.61% increase in the growth rate of hydrate after nucleation compared to the system without methionine. This concentration is very close to the methionine concentration (0.56 wt%) observed to have a promoting effect in previous CO_2 hydrate growth tests, again demonstrating consistency in the results. Our analysis results show that during the growth process, the side of the hydrate with methionine nearby grows faster, indicating the potential contribution of methionine to the growth of CO_2 hydrate.

Keywords:

Molecular dynamics simulation, Carbon dioxide hydrate, Amino acid, Methionine, Kinetic hydrate promoter

doi:10.6342/NTU202403841

CONTENTS

doi:10.6342/NTU202403841

doi:10.6342/NTU202403841

doi:10.6342/NTU202403841

doi:10.6342/NTU202403841

LIST OF FIGURES

doi:10.6342/NTU202403841

doi:10.6342/NTU202403841

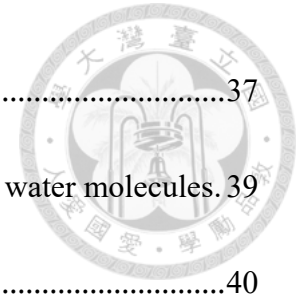

doi:10.6342/NTU202403841

doi:10.6342/NTU202403841

doi:10.6342/NTU202403841

doi:10.6342/NTU202403841

doi:10.6342/NTU202403841

LIST OF TABLES

doi:10.6342/NTU202403841

doi:10.6342/NTU202403841

Chapter 1 Introduction

1.1 Clathrate Hydrates

Clathrate hydrates, also known as gas hydrates, are formed due to the occupancy of guest molecules in polyhedral cavities caused by the hydrogen bonding interactions between water molecules, and common guest molecules include CH_4, CO_2, Ar, N_2, and so on.

Clathrate hydrates typically include three types of structures: sI, sII, and sH. Structure I (sI) hydrate consists of two 5^{12} small cages and six $5^{12}6^2$ large cages, containing 46 water molecules and 8 guest molecules. Structure II (sII) hydrate consists of sixteen 5^{12} small cages and eight $5^{12}6^4$ large cages, containing 136 water molecules and 24 guest molecules. Structure H (sH) hydrate consists of three 5^{12} small cages, two $4^35^66^3$ medium cages, and one $5^{12}6^8$ large cage, containing 34 water molecules and 6 guest molecules [1]. The schematic diagram of these three types of clathrate hydrate structures and common guest molecules is shown in Figure 1.1-1 [1]. Additional detailed information about clathrate hydrate structure can be found in Table 1.1-1 [2]. This research primarily focuses on the sI CO_2 hydrates.

doi:10.6342/NTU202403841

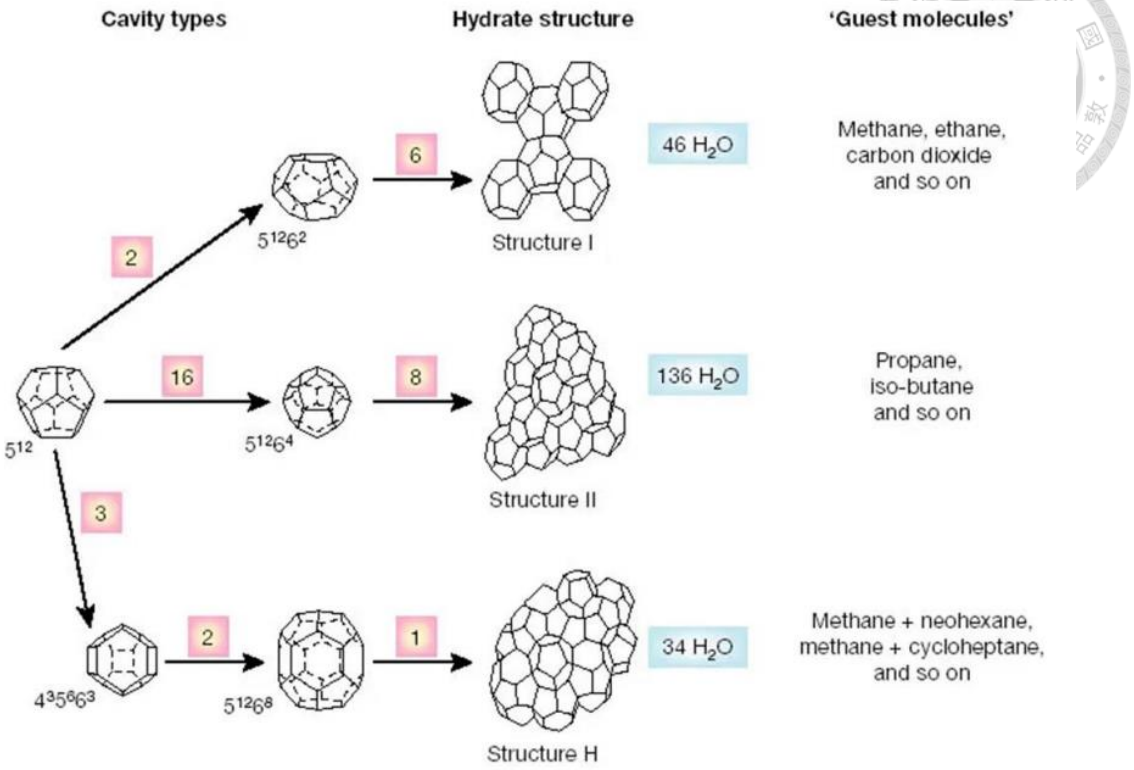

Figure 1.1-1 Clathrate hydrate composition and common guest molecules. [1]

Table 1.1-1 Geometry of cages in different hydrate structure. [2]

Structure	**I**		**II**		**H**		
Cavity	Small	Large	Small	Large	Small	Medium	Large
Description	5^{12}	$5^{12}6^2$	5^{12}	$5^{12}6^4$	5^{12}	$4^3 5^6 6^3$	$5^{12}6^8$
Number of cavities/unit cell	2	6	16	8	3	2	1
Average cavity radius (Å)	3.95	4.33	3.91	4.73	3.94	4.04	5.79
Variation in radius (%)	3.4	14.4	5.5	1.73	4.0	8.5	15.1
No. of water molecules/cavity	20	24	20	28	20	20	36

doi:10.6342/NTU202403841

1.2 Applications of Clathrate Hydrates

Clathrate hydrates are abundantly available worldwide, as shown in Figure 1.1-2 [3], and they have a wide range of applications. For example, methane hydrate is a significant energy source, prized for methane's effectiveness as a clean-burning fuel [4]. With its abundant reserves, methane hydrate provides a substantial energy supply [5-7]. Additionally, the hydrate form offers high methane density, which can provide greater economic profits in its transportation [1, 8, 9].

Furthermore, clathrate hydrates have potential future applications in hydrogen transport [10-13] and seawater desalination [14, 15]. They can even be used to sequester greenhouse gases such as CO_2, contributing to mitigating global warming [16-18]. Despite these advantages, clathrate hydrates also present challenges. Due to their tendency to form under high pressure and low temperature conditions, they can easily generate within pipelines for transporting natural gas in the deep sea, causing potential blockages [19]. Therefore, chemical inhibitors method or mechanical method must be used to prevent such occurrences [20-22].

doi:10.6342/NTU202403841

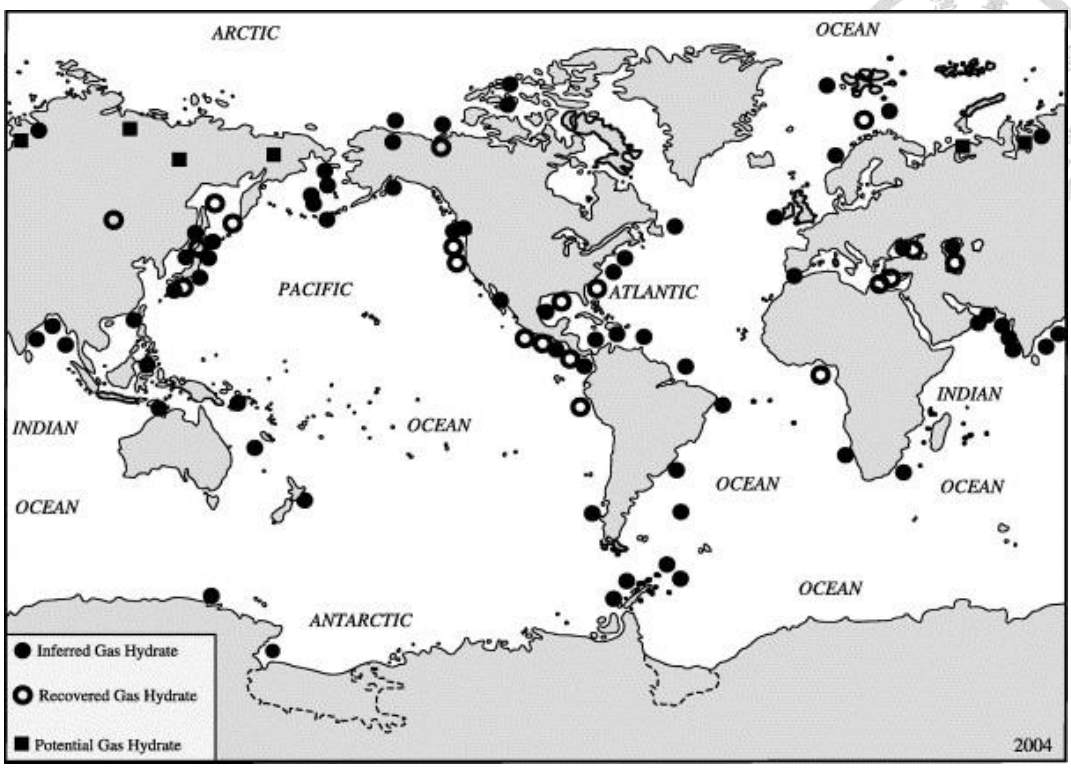

Figure 1.1-2 Distribution of gas hydrate around the world. [3]

1.3 Methionine

Methionine is a sulfur-containing amino acid essential for the human body and many other organisms, and it must be obtained through exogenous diet since it cannot be synthesized by the human body [23]. Methionine exists in two forms, L and D. In its natural state, methionine predominantly occurs as the L-form, as shown in Figure 1.2 [24]. Methionine has good water solubility, making it easily absorbed and metabolized in the body, so it participates in various metabolic pathways, including lipid metabolism, energy metabolism, and amino acid metabolism, playing a crucial role in maintaining overall

doi:10.6342/NTU202403841

health and regulating bodily functions [25].

Methionine is commonly used as a feed additive in the livestock and poultry industry and is also utilized in protein synthesis research. Additionally, due to its antioxidant properties, methionine is widely used in dietary supplements and food additives.

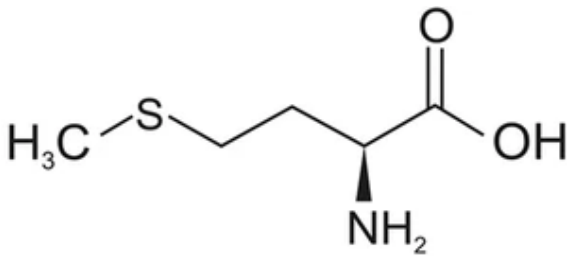

Figure 1.3-1 L-methionine molecule. [24]

1.4 Clathrate Hydrate Promoters

Clathrate hydrate promoters can be divided into two major categories: thermodynamic promoters and kinetic promoters, distinguished by their different mechanisms in promoting hydrate growth.

Thermodynamic promoters achieve promotion by shifting the phase equilibrium curve of hydrate. In other words, they increase the driving force for hydrate formation while maintaining the original temperature and pressure conditions [26]. However, a drawback of thermodynamic promoters is their tendency to occupy the cage-like

doi:10.6342/NTU202403841

structures of clathrate hydrates during hydrate formation, thereby reducing the gas storage capacity of the clathrate hydrates [26]. Common thermodynamic promoters include tetrahydrofuran (THF) [27-29], cyclopentane [29, 30] and tetrabutylammonium bromide (TBAB) [31, 32], and Figure 1.4-1 [26] is a schematic diagram of THF as a thermodynamic promoter.

On the other hand, kinetic promoters typically don't significantly affect the phase equilibrium curve of hydrates. Instead, they facilitate the formation of clathrate hydrates by increasing the mass transfer rates of molecules in the systems or through other mechanisms, such as increasing the solubility of guest molecules. Unlike thermodynamic promoters, kinetic promoters don't have the disadvantage of occupying the cage-like structures in clathrate hydrates [26]. The most common kinetic promoter is sodium dodecyl sulfate (SDS) [33, 34], and Figure 1.4-2 is a schematic diagram of SDS as a kinetic promoter.

In recent years, the researches on kinetic hydrate promoters have been steadily increasing. Fueled by a growing environmental awareness, some researchers have delved into the development of environmentally friendly kinetic hydrate promoters, and these environmentally friendly promoters often consist of amino acids [35-40] and biosurfactants [41, 42]. Furthermore, amino acids as promoters have an advantage over

doi:10.6342/NTU202403841

surfactants. When using surfactants like SDS, the formed hydrate tends to produce a large amount of foam upon decomposition [35]. In contrast, hydrates formed with amino acid promoters don't exhibit this foaming phenomenon during decomposition.

So far, methionine also has been confirmed by multiple studies as a kinetic hydrate promoter for CO_2 hydrate [37-40]. In the study by Cai et al. [37], their experimental results show that an aqueous solution of 0.2 wt% L-methionine at initial conditions of 273.2 K and 33 bar has a CO_2 gravimetric capacity far higher than that of a pure water system within the same duration (L-methionine solution system: 356 mg CO_2/g H_2O, pure water system: 81 mg CO_2/g H_2O), as shown in Figure 1.4-3. Additionally, its t_{90} (the time needed to reach 90% of their capacity) is also shorter compared to the pure water system, demonstrating its promoting effect on CO_2 hydrate formation. Moreover, in the study by Liu et al. [39], the promoting effects of methionine and SDS on CO_2 hydrates nucleation and growth are compared. The experimental results show that in the system containing methionine aqueous solution, at initial conditions of 293.2 K and 46 bar, the shortest induction time for nucleation is 311.70±148.07 minutes at 0.1 wt% methionine system, which is longer than the 61.42±19.86 minutes observed at system with 0.2 wt% SDS, but it is still much shorter than the pure water system's induction time of more than 2 days, as shown in Figure 1.4-4. In terms of hydrate growth, across the three concentrations of

doi:10.6342/NTU202403841

additives tested, the methionine-added system significantly outperforms the SDS-added system in both gas uptake limit and t_{90}, as shown in Figure 1.4-5.

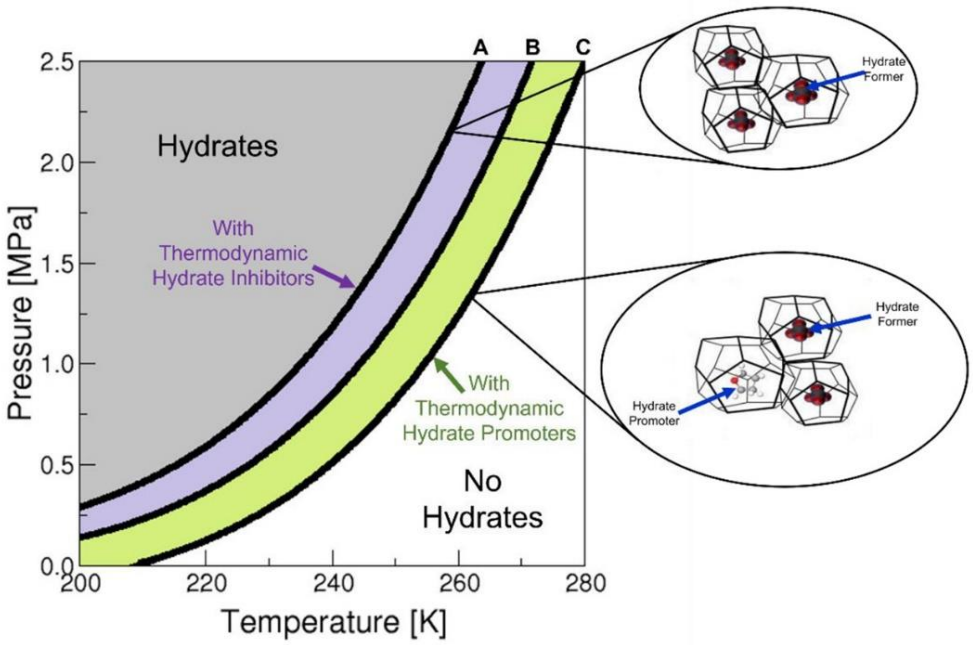

Figure 1.4-1 Schematic diagram of THF as a thermodynamic promoter. [26]

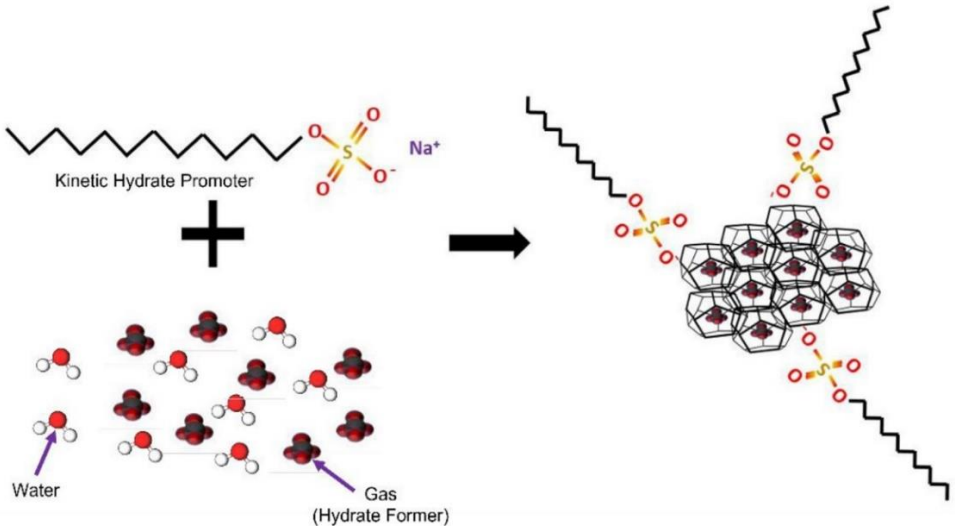

Figure 1.4-2 Schematic diagram of SDS as a kinetic promoter. [26]

doi:10.6342/NTU202403841

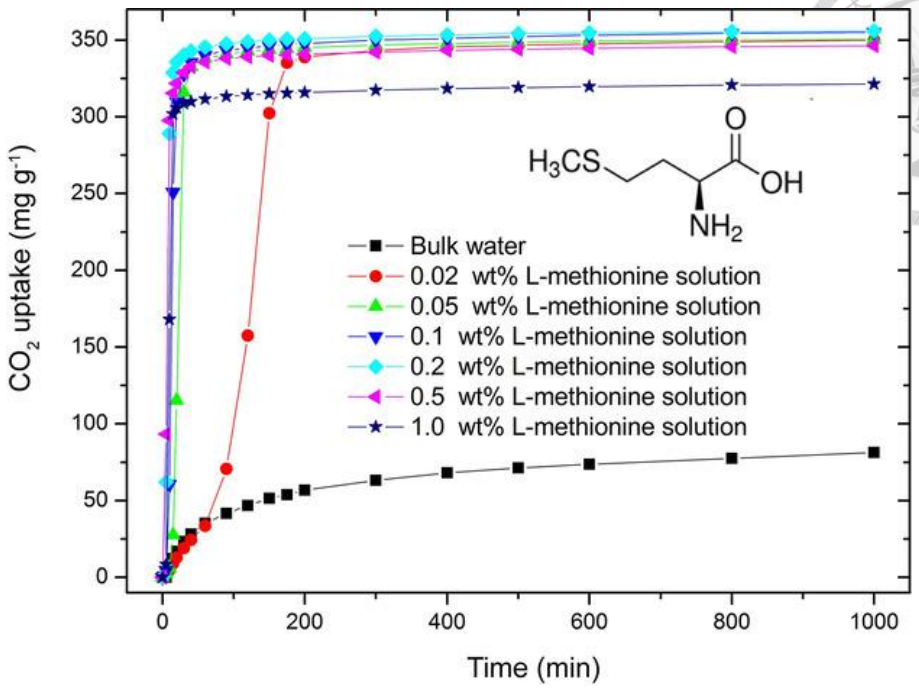

Figure 1.4-3 The CO_2 uptake kinetics for bulk water and methionine solutions (initial condition: 33 bar and 273.2 K). [37]

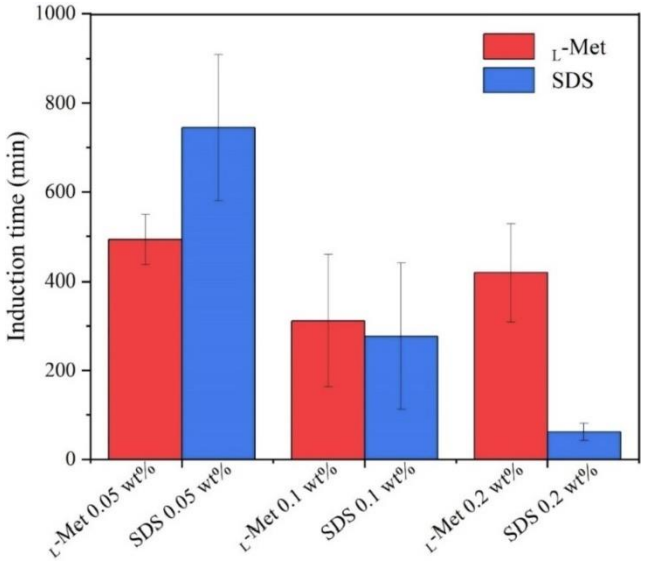

Figure 1.4-4 The comparison of induction times between systems with different concentrations of methionine and SDS. [39]

doi:10.6342/NTU202403841

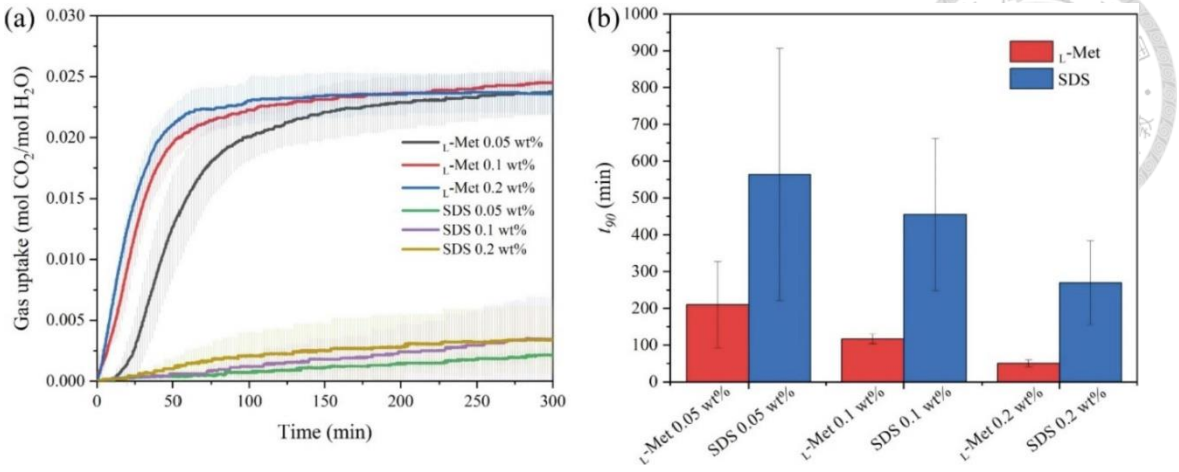

Figure 1.4-5 The comparison of gas uptake kinetics and t_{90} between systems with different concentrations of methionine and SDS. (a) Gas uptake kinetics. (b) t_{90}. [39]

1.5 Motivation

With the increasing severity of global warming, the ability of CO_2 hydrates to sequester CO_2, a greenhouse gas, has garnered significant attention. However, under conditions other than high pressure and low temperature, the formation rate of hydrates is quite slow, making the presence of promoters crucial. Although common kinetic hydrate promoters like SDS are currently available, amino acids as promoters have gained attention in recent years due to their environmental friendliness and the fact that hydrates formed with amino acids don't produce significant foaming upon dissociation.

Consequently, many studies have investigated amino acids as CO_2 hydrate promoters, including research on methionine, as shown in Table 1.5-1. While numerous

doi:10.6342/NTU202403841

studies confirm that methionine can indeed promote the nucleation and growth rate of CO_2 hydrates, the underlying promotion mechanism remains unclear. Therefore, this study focuses on exploring the potential promotion mechanisms of methionine on CO_2 hydrate nucleation and growth through molecular dynamics simulations.

Table 1.5-1 Researches on methionine as a promoter of CO_2 hydrate. [37-39]

Researcher	**Methionine concentration**	**Hydrate nucleation**	**Hydrate growth**
Cai et al. [37]	0.02~1.0 wt%	N/A	Driving force: ΔP=12 bar Effects: Increasing amount of CO_2 uptake and decreasing t_{90} compared to the system with pure water.
Zhang et al. [38]	0.015~0.179 wt%	N/A	Driving force: ΔP=1.5 bar Effects: Increasing amount of CO_2 uptake and decreasing t_{90} compared to the system with pure water.
Liu et al. [39]	0.05~0.2 wt%	Driving force: ΔT=4 K Effects: Reducing the induction time compared to the systems with pure water and SDS additive.	Driving force: ΔP=11 bar Effects: Increasing amount of CO_2 uptake and decreasing t_{90} compared to the systems with SDS additive.

doi:10.6342/NTU202403841

Chapter 2 Theory

2.1 Molecular Dynamics Simulation

Molecular dynamics (MD) simulation is a powerful method used to observe molecular motion and interactions in a microscopic scale. By analyzing a large number of trajectories of molecules at the microscopic level, it can estimate many thermodynamic and kinetic properties of the system and explore the reasons behind changes in macroscopic properties influenced by microscopic motions of molecules.

MD simulation is based on Newton's second law of motion, and its main process is illustrated in Figure 2.1-1. First, an initial structural model is established that includes the positions of all atoms and the initial velocities are then assigned to the atoms. Based on the force field parameters and atomic positions, accelerations can be calculated, allowing the determination of the positions and velocities of the atoms at the next frame. Repeating these steps provides a complete simulation trajectory. Additionally, conditions such as temperature and pressure can be controlled during the simulation using ensembles like NVT or NPT, enabling more customized simulations.

doi:10.6342/NTU202403841

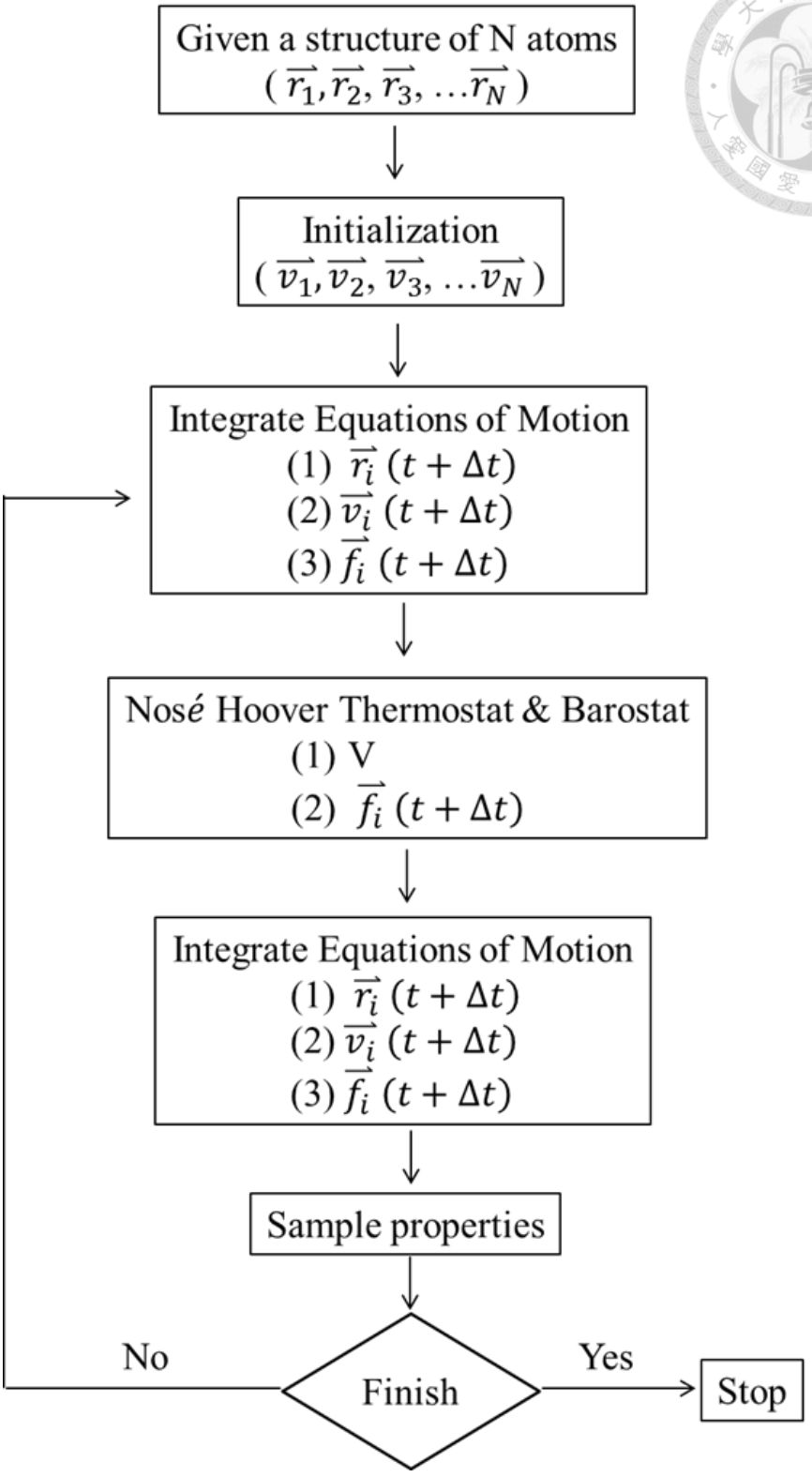

Figure 2.1-1 The flowchart of molecular dynamics simulation.

doi:10.6342/NTU202403841

2.2 Integration of Equation of Motion

The leap-frog integrator [43] is used to integrate the equation of motion in this study. From the atomic positions at time t, the acceleration (F(t)/m) can be determined, and the velocities and positions of each atom at the next time step can be calculated using Equations (2.2-1) and (2.2-2).

$$v(t+\frac{1}{2}\Delta t) = v(t-\frac{1}{2}\Delta t) + \frac{\Delta t}{m}F(t) \quad (2.2\text{-}1)$$

$$r(t+\Delta t) = r(t) + v(t+\frac{1}{2}\Delta t)\,\Delta t \quad (2.2\text{-}2)$$

2.3 Force Field

2.3.1 Overview

In molecular dynamics simulation, the interaction forces between any two atoms can be calculated using the selected force field parameters and atomic position information. From the potential energy, the interaction force between atoms can then be calculated, as shown in Equation (2.3.1-1).

$$-\frac{\partial U(t)}{\partial r_i} = F(t) \quad (2.3.1\text{-}1)$$

The overall potential energy of system is the sum of the non-bonded term ($E_{non-bond}$) and the valence term ($E_{valence}$), as shown in Equation (2.3.1-2).

$$U = E_{non-bond}+E_{valence} = E_{vdw}+E_{coul}+E_{bond}+E_{angle}+E_{dihedral} \quad (2.3.1\text{-}2)$$

doi:10.6342/NTU202403841

The van der Waals interaction (E_{vdw}) and the Coulomb interaction (E_{coul}) belong to the non-bonded terms, while the bond interaction (E_{bond}), angle interaction (E_{angle}), and torsion interaction ($E_{dihedral}$) belong to the valence terms. Within a molecule, non-bonded interactions between atoms separated by two or fewer valence bonds don't need to be considered, only bond and angle interactions are necessary. For atoms separated by three valence bonds, also known as 1-4 interaction, both non-bonded interactions and torsion interaction must be taken into account. As for atoms separated by four or more valence bonds, only non-bonded interactions need to be considered.

2.3.2 Non-Bonded Terms

The non-bonded interactions include van der Waals interaction (E_{vdw}) and Coulomb interaction (E_{coul}). The van der Waals interaction is composed of exchange-repulsive (repulsive) and dispersive (attractive) interactions, and they are described by the Lennard-Jones 12-6 function [44] in this research. The Lennard-Jones 12-6 function are defined in Equation (2.3.2-1), with the r_{ij}^{-12} term representing the repulsive component and the r_{ij}^{-6} term representing the attractive component. The parameters ϵ_{ij} and σ_{ij} represent the depth of the potential well and collision diameter, respectively.

$$E_{vdw}(r_{ij}) = 4\epsilon_{ij}[(\frac{\sigma_{ij}}{r_{ij}})^{12}-(\frac{\sigma_{ij}}{r_{ij}})^{6}] \quad (2.3.2\text{-}1)$$

doi:10.6342/NTU202403841

When considering the cross interaction between different atoms, the parameters ϵ_{ij} and σ_{ij} are typically obtained by the combination rules as shown in Equation (2.3.2-2) and (2.3.2-3).

$$\epsilon_{ij} = \sqrt{\epsilon_{ii}\epsilon_{jj}} \quad (2.3.2\text{-}2)$$

$$\sigma_{ij} = \sqrt{\sigma_{ii}\sigma_{jj}} \quad (2.3.2\text{-}3)$$

To increase computational efficiency during simulations, a cut-off radius (r_c) is usually set. This cut-off radius is sufficiently long to allow us to ignore the contribution of the repulsive component in the long-range region. Therefore, the long-range corrections of the Lennard-Jones potential only account for the dispersive component. For a plain cut-off, the dispersion energy and pressure caused by long-range dispersive interactions are shown in Equation (2.3.2-4) and (2.3.2-5) [45].

$$V_{lr} = -\frac{2}{3}\pi N\rho C_6 r_c^{-3} \quad (2.3.2\text{-}4)$$

$$P_{lr} = -\frac{4}{3}\pi C_6 \rho^2 r_c^{-3} \quad (2.3.2\text{-}5)$$

Another type of non-bonded interaction is Coulomb interaction, which describes the electrostatic energy of atoms as shown in Equation (2.3.2-6).

$$E_{coul}(r_{ij}) = \frac{q_i q_j}{4\pi\varepsilon_0 r_{ij}} \quad (2.3.2\text{-}6)$$

Because the Coulomb interaction of point charges doesn't converge in periodic boundary systems, the Ewald summation method proposed by Ewald et al. [46] is used to

doi:10.6342/NTU202403841

address this issue. This method allows for the efficient summation of electrostatic interactions between particles in the simulation box or their infinite periodic images by splitting the Coulomb interaction into two parts: the short-range part and the long-range part, and then they can converge quickly in real space and reciprocal space, respectively, as shown in Figure 2.3.2-1.

By reorganizing the replica sum, the Coulomb interaction is given by Equation (2.3.2-7).

$$E_{coul}(r_{ij})=\frac{1}{2}\sum_{m}^{\infty}\sum_{i=1}^{N}\sum_{j=1}^{N}\frac{q_i q_j \operatorname{erfc}(\sqrt{\alpha}r_{ij})}{|r_{ij}+mL|}+\frac{1}{2V}\sum_{k\neq 0}\sum_{i=1}^{N}\sum_{j=1}^{N}\frac{4\pi}{k^2}q_i q_j e^{-ikr_{ij}}e^{-\left(\frac{k^2}{4\alpha}\right)}-\frac{\alpha^{1/2}}{\pi}\sum_{i=1}^{N}q_i^2 \qquad (2.3.2\text{-}7)$$

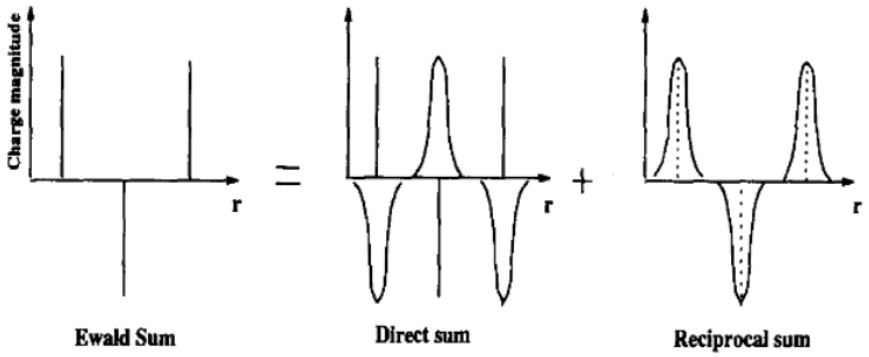

Figure 2.3.2-1 The component of Ewald summation. [46]

2.3.3 Valence Terms

The valence terms include bond interaction (E_{bond}), angle interaction (E_{angle}), and torsion interaction ($E_{dihedral}$), which describe the interactions between bonded atoms.

doi:10.6342/NTU202403841

Both the bond and angle interactions can be conceptualized as a harmonic motion, so the bond stretching energy and angle bending energy are described by Hooke's law in MD simulation, as shown in Equation (2.3.3-1) and (2.3.3-2), respectively. The l_0 represents the equilibrium bond length, θ_0 represents the equilibrium bond angle, and k_l and k_θ represent the force constants.

$$E_l = \frac{1}{2}k_l(l-l_0)^2 \quad (2.3.3\text{-}1)$$

$$E_\theta = \frac{1}{2}k_\theta(\theta-\theta_0)^2 \quad (2.3.3\text{-}2)$$

The potential energy variation caused by bond rotation is expressed by the dihedral term, as shown in Equation (2.3.3-3), where ϕ_s represents the dihedral angle with the highest energy.

The torsion energy, which pertains to the rotation of chemical bonds, depends on the dihedral angles between valence bonds. This energy can be simplified to Equation (2.3.3-3), where ϕs represents the dihedral angle with the highest structural energy.

$$E_{dihedral} = k_\phi \cos m(\phi-\phi_s) \quad (2.3.3\text{-}3)$$

2.4 Ensemble

The concept of ensemble was first introduced into statistical thermodynamics by J.Willard Gibbs [47]. Due to the differences in microscopic details, such as particle

doi:10.6342/NTU202403841

velocities, which can affect the observed properties of a macroscopic system, we typically collect a large number of microscopic configurations with varying details in MD simulation, each configuration representing a possible state of the macroscopic system, and then calculate their statistical average to represent the thermodynamic properties of the macroscopic system. This approach provides results that are close to direct measurements in macroscopic systems and is known as ensemble averaging [48]. Various types of ensembles can satisfy different macroscopic constraints. In this study, the canonical ensemble (NVT) that simulates the closed system with fixed volume isothermally and the isothermal-isobaric ensemble (NPT) that simulates the closed system with fixed pressure isothermally are utilized.

2.5 Temperature Thermostat

The temperature control method used in this study is the Nosé-Hoover thermostat [49, 50], which is employed to simulate the scenario of controlling the system temperature with a heat bath. The equations of motion for the particles and the heat bath parameter ξ are given by Equations (2.5-1) and (2.5-2), respectively. In these equations, Q is the mass parameter of heat bath, P_ξ is momentum of friction parameter, T is the instantaneous system temperature, and T_0 is the reference temperature.

doi:10.6342/NTU202403841

$$\frac{d^2 r_i}{dt^2} = \frac{F_i}{m_i} - \frac{P_\xi}{Q}\frac{dr_i}{dt} \quad (2.5\text{-}1)$$

$$\frac{dp_\xi}{dt} = (T\text{-}T_0) \quad (2.5\text{-}2)$$

2.6 Pressure Barostat

Two pressure control methods are utilized in this study. The first method is the Berendsen barostat [51], which adjusts the coordinates and box vectors at each step (n_{pc}) using a scaling matrix μ with a first-order relaxation effect, aiming to approach the set reference pressure. This adjustment is described by Equation (2.6-1) and the scaling matrix μ is given by Equation (2.6-2). β_{ij} represents the isothermal compressibility of the system. Although this method can provide the correct average system pressure, it is unable to produce the exact NPT ensemble.

$$\frac{dP}{dt} = \frac{P_0\text{-}P}{\tau_p} \quad (2.6\text{-}1)$$

$$\mu_{ij} = \delta_{ij} - \frac{n_{PC}\Delta t}{3\tau_p}\beta_{ij}\{P_{0ij} - P_{ij}(t)\} \quad (2.6\text{-}2)$$

The second method is the Parrinello-Rahman barostat [52]. In this method, the adjustment of the box vectors (b) follows a matrix equation of motion, as described by Equation (2.6-3). V is the volume of the simulation box, W is a matrix parameter determining the coupling strength, and the matrices P and P_{ref} correspond to the current pressure and the reference pressure, respectively. This method provides the true NPT

doi:10.6342/NTU202403841

ensemble, and thus all NPT simulations for the data analysis in this study were performed using it.

$$\frac{db^2}{dt^2} = VW^{-1}b'^{-1}(P-P_{ref}) \quad (2.6\text{-}3)$$

doi:10.6342/NTU202403841

Chapter 3 Computational details

3.1 Settings

In this study, the initial models for MD simulations are constructed by Materials Studio 5.0 [53], and all the simulations are conducted using GROMACS 4.5.5 [54]. During the simulations, the leap-frog algorithm [43] is used to integrate the Newton's equations of motion with a time step of 1 fs. Lennard-Jones potential [44] is used to describe van der Waals interaction, and dispersion correction [45] and Particle-Mesh Ewald (PME) method [46] are used to calculation the long-range contributions of van der Waals and Coulomb interactions respectively. The cut-off radiuses for van der Waals and Coulomb interactions are set to 1.0 nm. The time constant (τ_t) for the Nosé-Hoover thermostat [49, 50] is 1 ps, while the time constant (τ_p) for the Berendsen barostat [51] and Parrinello-Rahman barostat [52] is 10 ps.

The MD simulation process in this research consists of two major parts: pre-equilibrium and target simulation, as shown in Figure 3.1-1. In the pre-equilibrium part, the system energy is first minimized, and then an NVT simulation of 200 ps is performed at a temperature of 200 K for relaxing extra stress in the system. Subsequently, the temperature is increased from 200 K to the target temperature with a heating rate of 0.5 K/ps and an extra 100 ps simulation is conducted at target temperature in the NPT

doi:10.6342/NTU202403841

simulation using the Berendsen barostat for achieving equilibrium state quickly. At this point, the pre-equilibrium before the target simulation is completed. Finally, the target NPT simulation using the Parrinello-Rahman barostat is carried out at the target temperature.

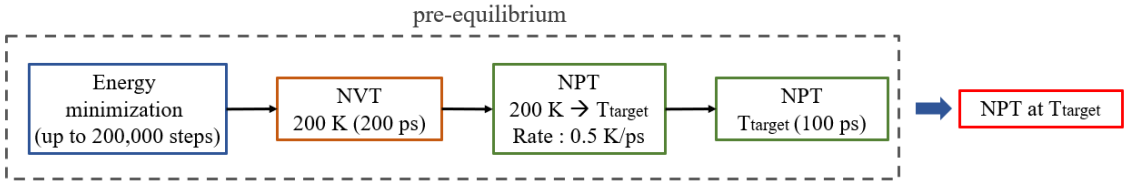

Figure 3.1-1 The flowchart of MD simulation process in this research.

3.2 Models

The initial structures of each simulation system are shown in Table 3.2-1. The series A models are for CO_2 solubility tests, series B models are for diffusivity tests, series C models are for heat of dissociation of CO_2 hydrate tests, series D models are for CO_2 hydrate melting point tests, series E models are for CO_2 hydrate growth tests, and series F models are for CO_2 hydrate nucleation tests. The position information for unit cell of perfect structure I hydrate are from Takeuchi et al [55]. The methionine molecules in all models are in their zwitterionic form [56]. This is because the carboxyl and amino group of methionine correspond to pKa values of 2.13 and 9.27 [57], respectively, causing the

doi:10.6342/NTU202403841

carboxyl group to deprotonate and the amino group to protonate in a neutral aqueous solution.

Table 3.2-1 Initial structures of each simulation system.

Model	**Usage**	**Composition**
A1 (Figure 3.2-1)	4.1.1, 4.2.2	Two slabs: a liquid phase of 1000 water molecules and a gas phase of 500 CO_2 molecules.
A2 (Figure 3.2-2)	4.2.2	Two slabs: a liquid phase of 1000 water molecules and 2 methionine molecules, and a gas phase of 500 CO_2 molecules.
A3 (Figure 3.2-3)	4.2.2	Two slabs: a liquid phase of 1000 water molecules and 4 methionine molecules, and a gas phase of 500 CO_2 molecules.
A4 (Figure 3.2-4)	4.2.2	Two slabs: a liquid phase of 1000 water molecules and 6 methionine molecules, and a gas phase of 500 CO_2 molecules.
A5 (Figure 3.2-5)	4.2.2	Two slabs: a liquid phase of 1000 water molecules and 8 methionine molecules, and a gas phase of 500

doi:10.6342/NTU202403841

		CO_2 molecules.
B1	4.1.2	Homogenous: a liquid phase of 2000 water molecules and 5 CO_2 molecules.
B2	4.3.2	Homogenous: a liquid phase of 1000 water molecules and 32 CO_2 molecules.
B3	4.3.2	Homogenous: a liquid phase of 1000 water molecules, 32 CO_2 molecules, and a methionine molecule.
B4	4.3.2	Homogenous: a liquid phase of 1000 water molecules, 32 CO_2 molecules, and 2 methionine molecules.
B5	4.3.2	Homogenous: a liquid phase of 1000 water molecules, 32 CO_2 molecules, and 4 methionine molecules.
B6	4.3.2	Homogenous: a liquid phase of 1000 water molecules, 32 CO_2 molecules, and 6 methionine molecules.
B7	4.3.2	Homogenous: a liquid phase of 1000 water

doi:10.6342/NTU202403841

		molecules, 32 CO_2 molecules, and 8 methionine molecules.
C1 (Figure 3.2-6)	4.1.3	(a) 2×2×2 unit cell of perfect sI CO_2 hydrate (b) Homogenous: a liquid phase of 368 water molecules and 64 CO_2 molecules.
D1 (Figure 3.2-7)	4.1.4	Four slabs: two liquid phases include 736 water molecules individually, the 2×2×3 unit cell of sI CO_2 hydrate with 0.5 small cage occupancy separates the liquid phases, and a gas phase of 512 CO_2 molecules.
D2 (Figure 3.2-8)	4.2.1	Four slabs: two liquid phases include 736 water molecules individually, the 2×2×2 unit cell of sI CO_2 hydrate with 0.5 small cage occupancy separates the liquid phases, and a gas phase of 256 CO_2 molecules.
D3 (Figure 3.2-9)	4.2.1	Four slabs: two liquid phases include 736 water molecules and 2 methionine molecules individually, the 2×2×2 unit cell of sI CO_2 hydrate with 0.5 small cage occupancy separates the liquid phases, and a gas phase of 256 CO_2 molecules.

doi:10.6342/NTU202403841

D4 (Figure 3.2-10)	4.2.1	Four slabs: two liquid phases include 736 water molecules and 4 methionine molecules individually, the 2×2×2 unit cell of sI CO_2 hydrate with 0.5 small cage occupancy separates the liquid phases, and a gas phase of 256 CO_2 molecules.
D5 (Figure 3.2-11)	4.2.1	Four slabs: two liquid phases include 736 water molecules and 6 methionine molecules individually, the 2×2×2 unit cell of sI CO_2 hydrate with 0.5 small cage occupancy separates the liquid phases, and a gas phase of 256 CO_2 molecules.
E1 (Figure 3.2-12)	4.2.3, 4.2.4	Three slabs: two liquid phases include 736 water molecules and 74 CO_2 molecules individually, and the 2×2×2 unit cell of sI CO_2 hydrate with 0.5 small cage occupancy separates the liquid phases.
E2 (Figure 3.2-13)	4.2.4	Three slabs: two liquid phases include 736 water molecules and 74 CO_2 molecules individually, a methionine molecule in one of the liquid phases, and the 2×2×2 unit cell of sI CO_2 hydrate with 0.5 small

doi:10.6342/NTU202403841

		cage occupancy separates the liquid phases.
E3 (Figure 3.2-14)	4.2.4	Three slabs: two liquid phases include 736 water molecules, 74 CO_2 molecules and a methionine molecule individually, and the 2×2×2 unit cell of sI CO_2 hydrate with 0.5 small cage occupancy separates the liquid phases.
E4 (Figure 3.2-15)	4.2.3, 4.2.4	Three slabs: two liquid phases include 736 water molecules, 74 CO_2 molecules and 2 methionine molecules individually, and the 2×2×2 unit cell of sI CO_2 hydrate with 0.5 small cage occupancy separates the liquid phases.
E5 (Figure 3.2-16)	4.2.3, 4.2.4	Three slabs: two liquid phases include 736 water molecules, 74 CO_2 molecules and 4 methionine molecules individually, and the 2×2×2 unit cell of sI CO_2 hydrate with 0.5 small cage occupancy separates the liquid phases.
E6 (Figure 3.2-17)	4.2.3, 4.2.4	Three slabs: two liquid phases include 736 water molecules, 74 CO_2 molecules and 6 methionine

doi:10.6342/NTU202403841

		molecules individually, and the 2×2×2 unit cell of sI CO_2 hydrate with 0.5 small cage occupancy separates the liquid phases.
F1	4.4.2	Homogenous: a liquid phase of 1000 water molecules and 150 CO_2 molecules.
F2	4.4.2	Homogenous: a liquid phase of 1000 water molecules, 150 CO_2 molecules and a methionine molecule.
F3 (Figure 3.2-18)	4.4.3	Two slabs: a liquid phase of 1242 water molecules and a gas phase of 216 CO_2 molecules.
F4 (Figure 3.2-19)	4.4.3	Two slabs: a liquid phase of 1242 water molecules and a methionine molecule and a gas phase of 216 CO_2 molecules.

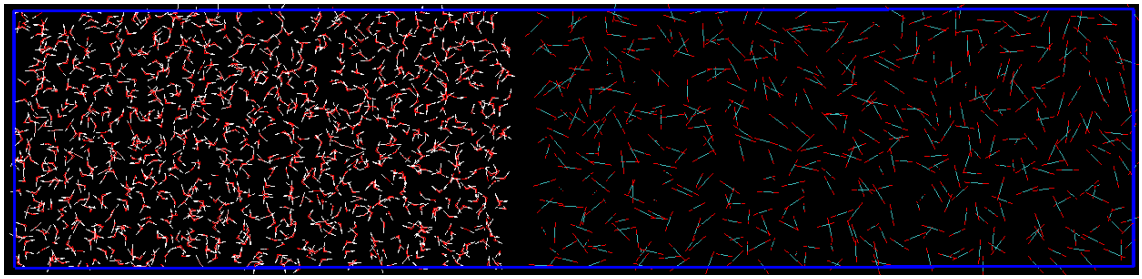

Figure 3.2-1 Model A1.

doi:10.6342/NTU202403841

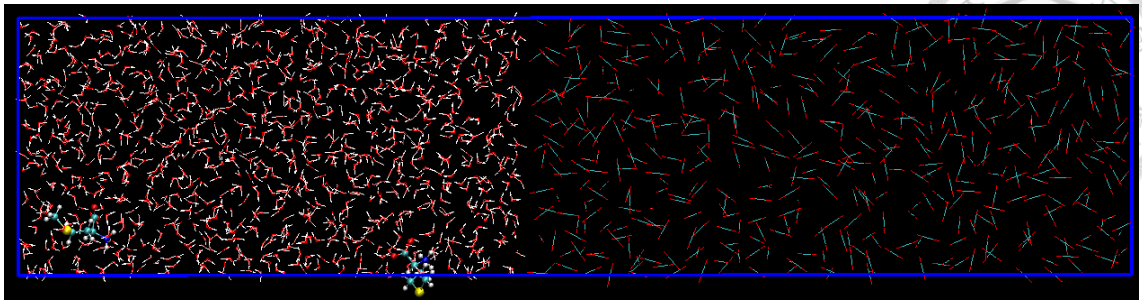

Figure 3.2-2 Model A2.

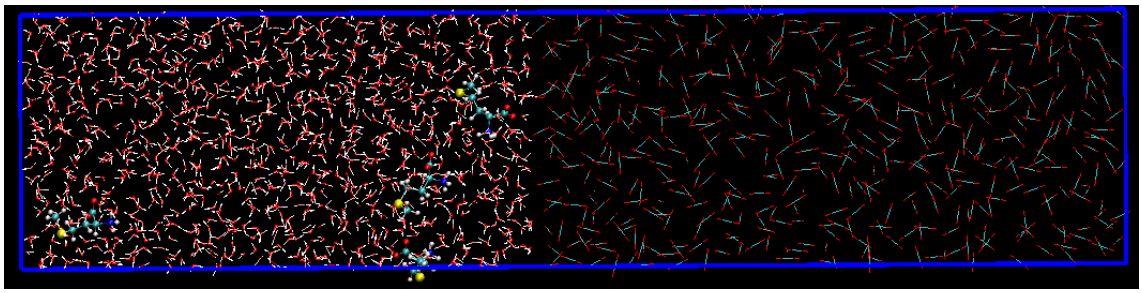

Figure 3.2-3 Model A3.

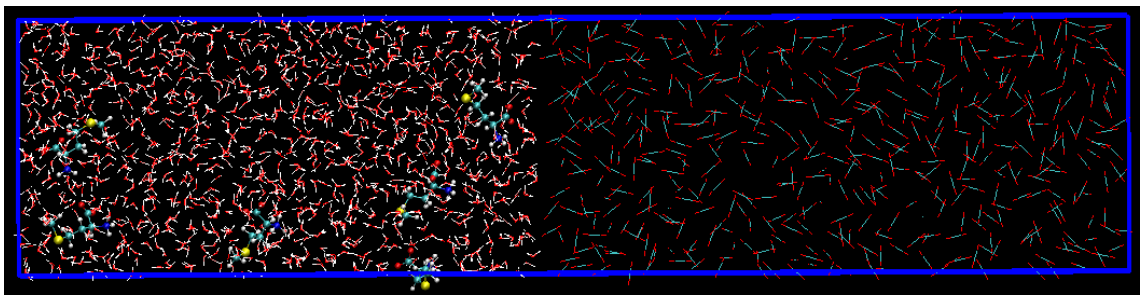

Figure 3.2-4 Model A4.

doi:10.6342/NTU202403841

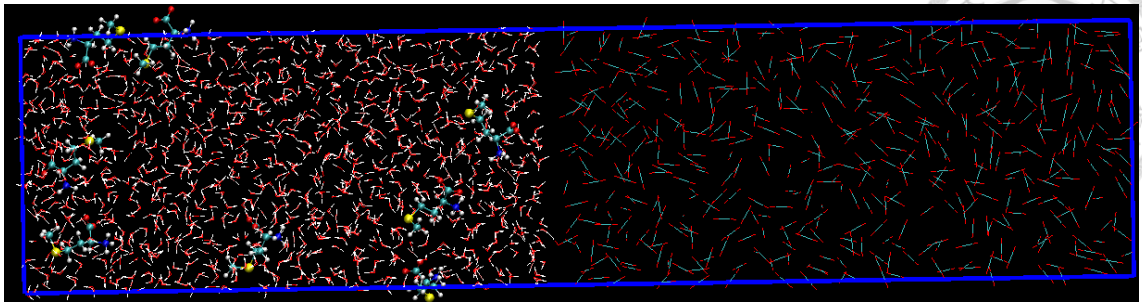

Figure 3.2-5 Model A5.

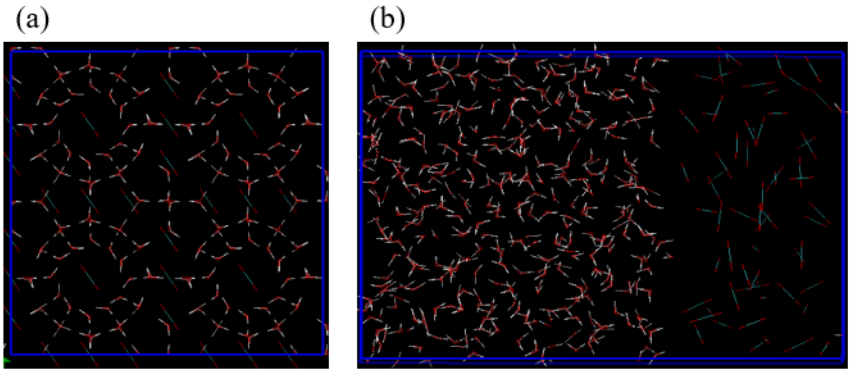

Figure 3.2-6 Model C1.

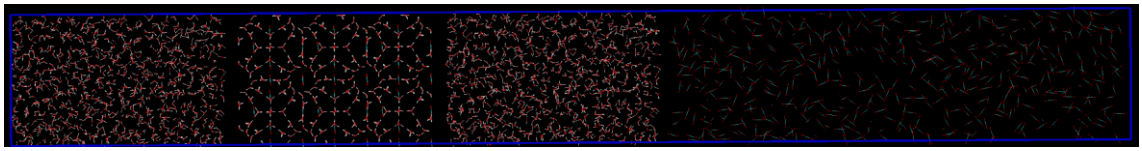

Figure 3.2-7 Model D1.

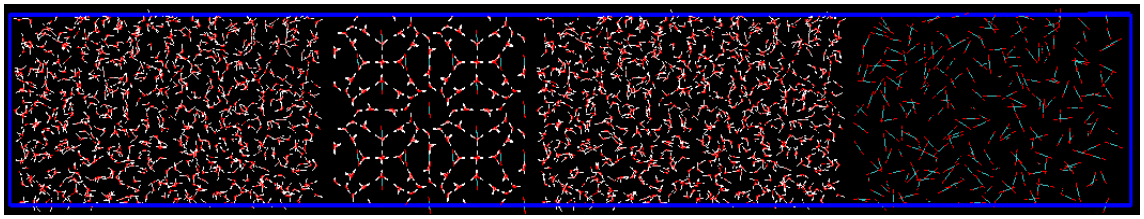

Figure 3.2-8 Model D2.

doi:10.6342/NTU202403841

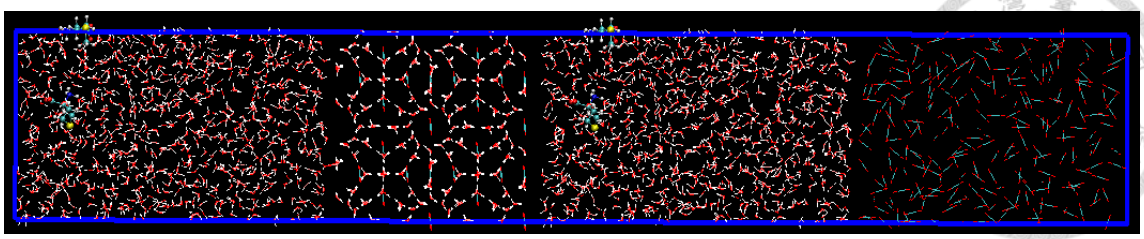

Figure 3.2-9 Model D3.

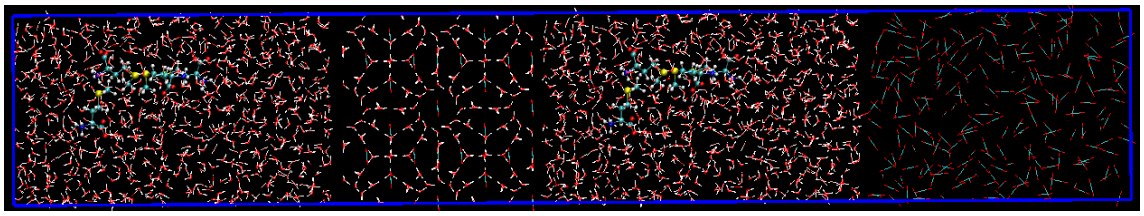

Figure 3.2-10 Model D4.

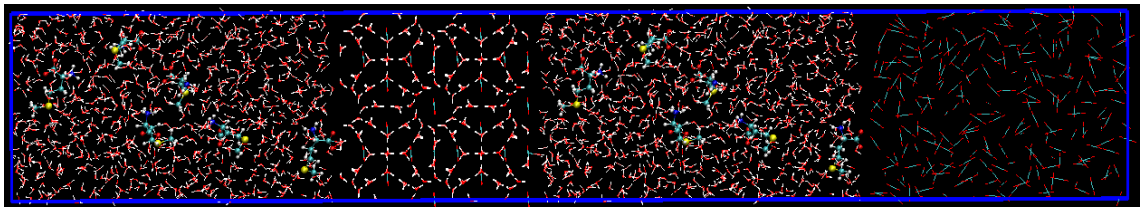

Figure 3.2-11 Model D5.

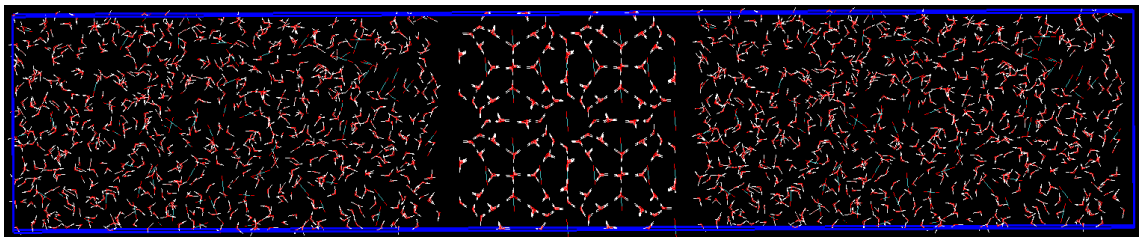

Figure 3.2-12 Model E1.

doi:10.6342/NTU202403841

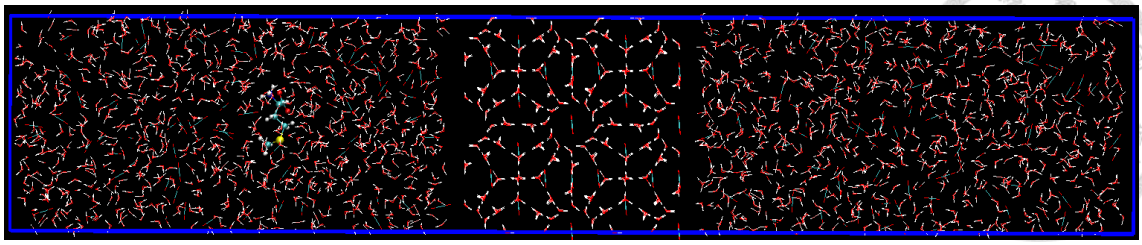

Figure 3.2-13 Model E2.

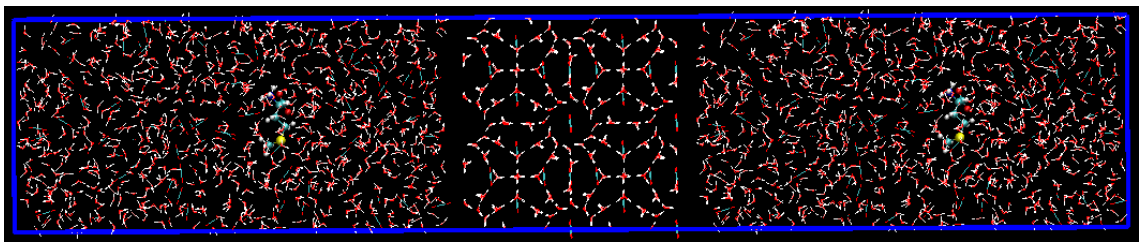

Figure 3.2-14 Model E3.

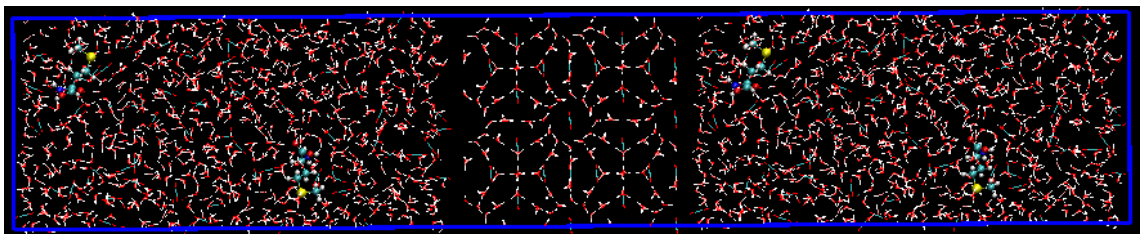

Figure 3.2-15 Model E4.

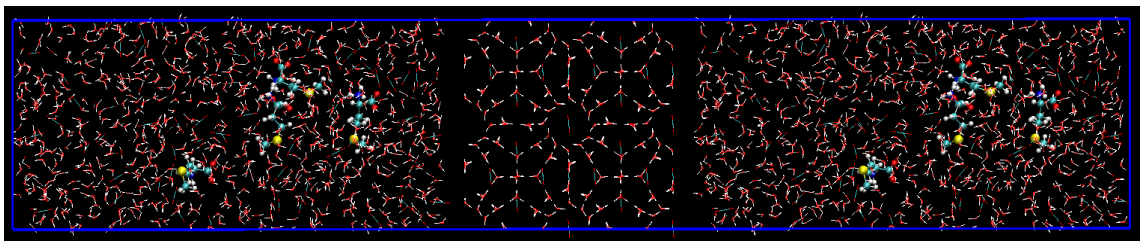

Figure 3.2-16 Model E5.

doi:10.6342/NTU202403841

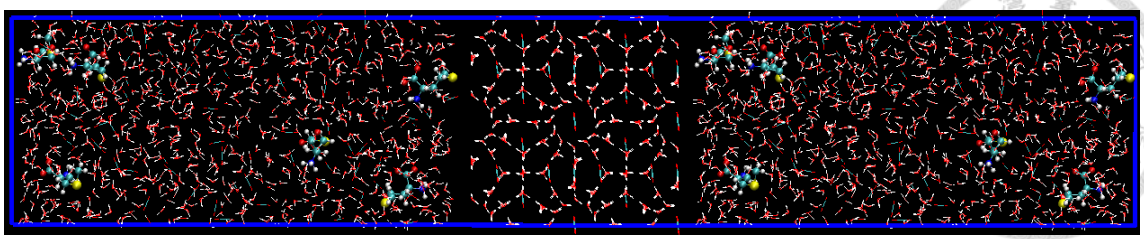

Figure 3.2-17 Model E6.

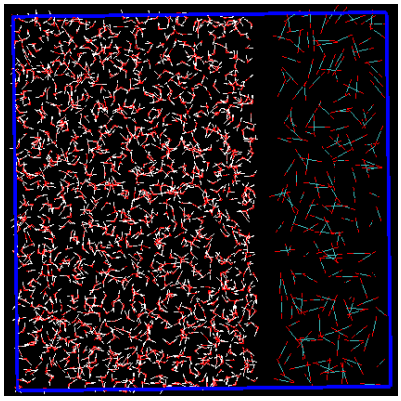

Figure 3.2-18 Model F3.

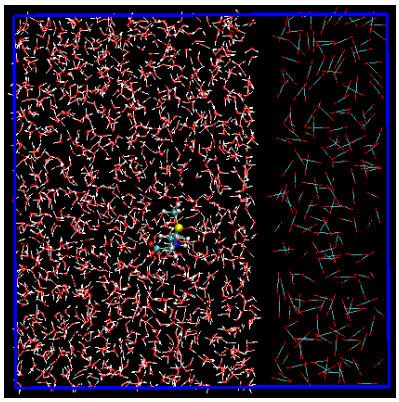

Figure 3.2-19 Model F4.

doi:10.6342/NTU202403841

3.3 Force Field

The force field used to describe water molecules in the system is the TIP4P/Ice model [58], and the CO_2 molecules are described using the EPM2 model [59]. For methionine molecules, the parameters of OPLS-AA model are from LigParGen [60-62], and the molecular structure of methionine is shown in Figure 3.3-1. The force field parameters for the three types of molecules are shown in Table 3.3-1 [58-62]. To enhance the interaction between water and CO_2 molecules, the Lennard-Jones parameters ϵ_{ij} for the non-bonded interactions between them were modified as shown in Equation (3.3-1) [63]. The Lennard-Jones and electrostatic potentials for 1-4 non-bonded interactions are scaled by a factor of 0.5.

$$\epsilon_{ij} = 1.1\sqrt{\epsilon_{ii}\epsilon_{jj}} \tag{3.3-1}$$

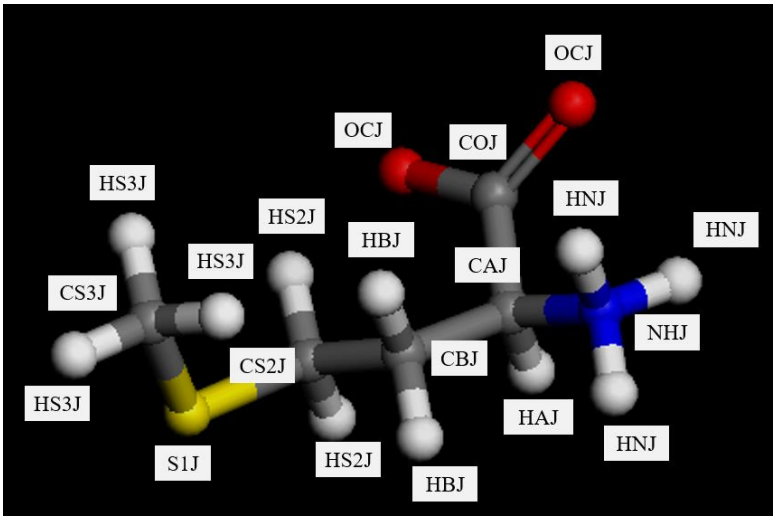

Figure 3.3-1 Molecular structure of methionine.

doi:10.6342/NTU202403841

Table 3.3-1 Force field parameters. [58-62]

Molecule	**Atom**	**ϵ (kJ/mol)**	**σ (nm)**	**q (e)**
H_2O	O	0.881949	0.316685	0.0000
	H	0	0	0.5897
	MW	0	0	-1.1794
CO_2	C	0.233865	0.2757	0.6512
	O	0.669335	0.3033	-0.3256
Methionine	CS2J (C)	0.35	0.276144	-0.1921
	HS2J (H)	0.25	0.12552	0.1887
	S1J (S)	0.36	1.48532	-0.2252
	CS3J (C)	0.35	0.276144	-0.2394
	HS3J (H)	0.25	0.12552	0.1187
	CBJ (C)	0.35	0.276144	-0.1986
	HBJ (H)	0.25	0.12552	0.1037
	CAJ (C)	0.35	0.276144	-0.0398
	COJ (C)	0.355	0.29288	0.3326
	OCJ (O)	0.296	0.87864	-0.6505
	HAJ (H)	0.25	0.12552	0.1754
	NHJ (N)	0.325	0.71128	-0.5563
	HNJ (H)	0	0	0.4345

doi:10.6342/NTU202403841

3.4 Hydrate Characteristic Determination

3.4.1 Four-body Order Parameter

The four-body order parameter, also known as the F4 order parameter, is a parameter used to determine the structural characteristic of water molecules. The definition of F4 order parameter is given by Equation (3.4.1) [64], with the required parameters shown in Figure 3.4.1-1. Here, R represents the distance between the oxygen atoms of two water molecules, and θ denotes the dihedral angle formed by the two farthest hydrogen atoms in the H-O…O-H arrangement. Retrieving water molecules staying around a center water molecule, if R ≤ 3.5 Å, the dihedral angle θ is calculated, and finally the average of all cos(3θ) values is taken as the F4 order parameter for that central water molecule.

In general, the F4 value for a water molecule is around -0.4 in the ice state, approximately -0.04 in the liquid water state, and around 0.7 in the hydrate state.

$$F4 = \langle \cos(3\theta) \rangle \qquad (3.4.1\text{-}1)$$

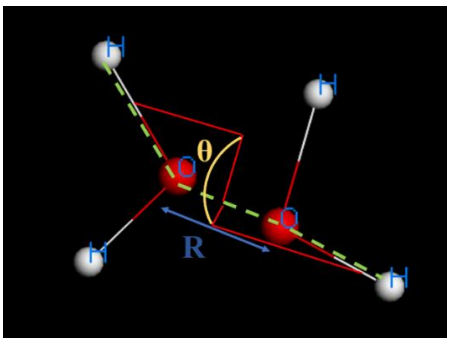

Figure 3.4.1-1 The geometry of F4 calculation.

doi:10.6342/NTU202403841

3.4.2 Hydrate-liquid Interface Determination

In this study, the hydrate-liquid interface is defined using the following method. First, we check whether water molecules undergo significant deformations in simulation. If the O-H bond length is shorter than 0.09 nm or the H-O-H bond angle is greater than 108 or less than 102 degrees, the water molecule is considered to have undergone deformation. When a water molecule undergoes deformation or has an F4 order parameter less than or equal to 0.6, it is classified as a liquid water neighbor. If a water molecule does not undergo deformation and has an F4 order parameter greater than 0.6, it is classified as a hydrate water neighbor.

Next, water molecules with F4 order parameters ranging from 0.3 to 0.9 are identified in the system. Using these water molecules as centers, the ratio of the number of liquid water neighbors to hydrate water neighbors within a distance of 3.5 Å along the z-axis is calculated. If this ratio falls between 0.5 and 2.5, the water molecule is considered to be at the hydrate-liquid interface.

After identifying all interface water molecules, the average z-coordinate value of those interface water molecules represents the z-axis position of the hydrate-liquid interface. The positions of interface water molecules are depicted as the blue water molecules in Figure 3.4.2-1.

doi:10.6342/NTU202403841

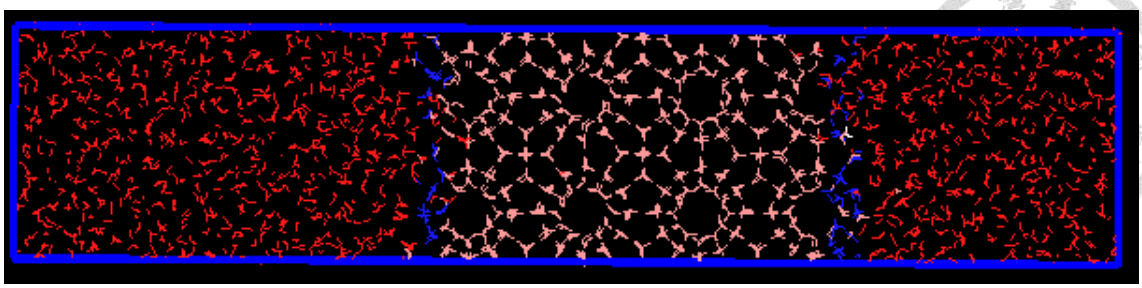

Figure 3.4.2-1 Schematic diagram for the positions of interface water molecules.

3.4.3 Mutually Coordinated Guest order parameter

The mutually coordinated guest (MCG) order parameter can sensitively and quantitatively analyze the nucleation and growth of clathrate hydrates by detecting the specific arrangement structures formed by guest molecules and water molecules in space [65]. The geometry of MCG calculation for CO_2 hydrate is shown in Figure 3.4.3-1, where the angle ϕ is 45°.

First, we should identify all neighboring guest molecules within a distance of 9 Å (R_g^{cut}) from a candidate guest molecule, and then we need to analyze the number of water molecules between the candidate and its neighboring guest molecules. If at least 5 water molecules in the system are within a distance of 6 Å (R_w^{cut}) from both the candidate and neighboring guest molecules and these water molecules also lie within the intersection of two 90° cones projected bidirectionally between the two guest molecules, the count value (Nc) of the candidate guest molecule is incremented by 1. When the Nc value exceeds at

doi:10.6342/NTU202403841

least 3, the candidate guest molecule is considered an MCG-3 monomer.

If two adjacent MCG-3 monomers also meet the aforementioned criteria with each other, they are considered to be in the same MCG-3 cluster. The number of MCG-3 monomers in the largest MCG-3 cluster in the system is taken as the MCG-3 order parameter value at that time.

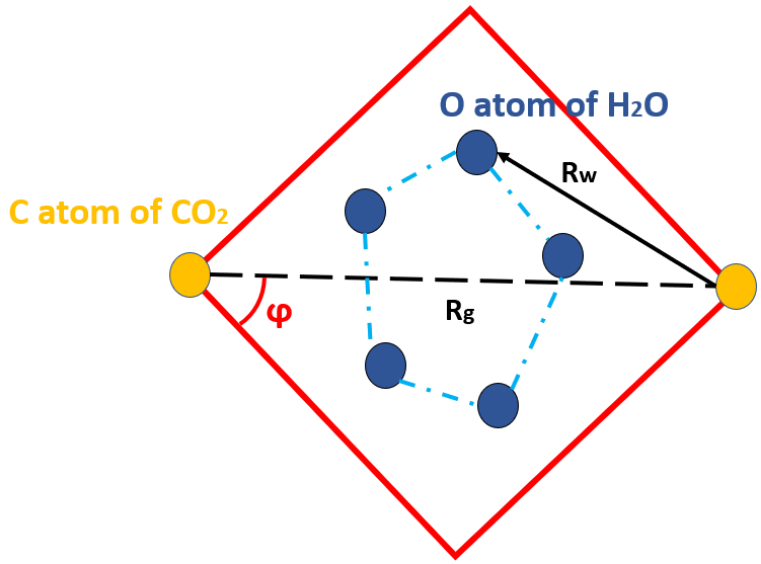

Figure 3.4.3-1 Geometry of MCG calculation for CO_2 hydrate.

3.4.4 Mean First-Passage Time Method

The mean first-passage time (MFPT) method [66] is a powerful technique that can precisely determine important properties during clathrate hydrate nucleation, such as nucleation rate and the critical cluster size, by analyzing only the kinetic information from molecular trajectories. Before using this method, multiple MD simulations of clathrate

doi:10.6342/NTU202403841

hydrate nucleation must be performed. For each independent simulation run, the MCG-3 order parameter is used to determine the size of the hydrate cluster. The first-passage time (τ) of each cluster size in different simulation runs are then averaged using Equation (3.4.4-1) [67] to produce the MFPT curve, this equation is based on the maximum likelihood estimate [68], where N_R is the number of simulations that can achieve or exceed the cluster size and N_{NR} is the number of remaining simulations.

$$\tau = \frac{\sum_{i=1}^{N_R} \tau_i + \sum_{k=1}^{N_{NR}} \tau_k}{N_R} \quad (3.4.4\text{-}1)$$

Once the MFPT curve is obtained, it can be fitted using Equation (3.4.4-2) [66], which provides information of induction time (τ_J), nucleation rate ($J = \frac{1}{V_{liq}\tau_J}$), critical cluster size (n*), and the Zeldovich factor (Z).

$$\tau(n) = 0.5\tau_J[1 + \mathrm{erf}(Z\sqrt{\pi}\,(n - n^*))] \quad (3.4.4\text{-}2)$$

However, Equation (3.4.4-2) is only applicable when the energy barrier of nucleation is quite high. If the energy barrier of nucleation is not sufficiently high, meaning the hydrate growth after nucleation is also not fast enough, the fitting of the MFPT curve by Equation (3.4.4-2) will be inaccurate. To achieve a better fit of the MFPT curve, Yi et al. [69] add an additional term related to the hydrate growth rate to Equation (3.4.4-2). The modified equation is shown as Equation (3.4.4-3), where G is the hydrate growth rate and H is the Heaviside function.

doi:10.6342/NTU202403841

$$\tau(n) = 0.5\tau_J \left[1 + \mathrm{erf}\left(Z\sqrt{\pi}\,(n - n^*)\right)\right] + G^{-1}(n - n^*)H(n - n^*) \quad (3.4.4\text{-}3)$$

doi:10.6342/NTU202403841

Chapter 4 Results and Discussion

4.1 Force Field Validation

4.1.1 CO_2 Solubility in Water

For testing the solubility of CO_2 in pure water, two 200 ns NPT simulations at 280 K, 285 K and 30 bar were conducted, and the initial system is shown in Model A1 (Figure 3.2-1). The solubility of CO_2 is calculated by dividing the simulation box into 50 equal-volume slices along the z-axis and then averaging the CO_2 solubility in each slice within the liquid phase region, which is obtained by dividing the number density of CO_2 by that of water over the selected equilibrium period (50~200 ns).

The simulation and experimental results [70] of CO_2 solubility are shown in Table 4.1.1-1, and the simulation results of CO_2 solubilities at 280 K and 285 K are approximately 27.39% and 40.51% higher than the experimental results, respectively. The results suggest that the attractive force between CO_2 and water molecules in the simulations is stronger than in reality, which would explain the increased CO_2 solubility observed in the simulations.

doi:10.6342/NTU202403841

Table 4.1.1-1 CO_2 solubility in pure water at 30 bar.

Condition	Simulation results (CO_2 molecules/100 water molecules)	Experimental results [70] (CO_2 molecules/100 water molecules)
280 K, 30 bar	3.186	2.501
285 K, 30 bar	3.014	2.145

4.1.2 CO_2 Diffusivity in Water

For the diffusivity of CO_2 in pure water, a 10 ns NPT simulation was conducted at 279 K and 1 atm, with the initial system shown in Model B1, and the trajectory in the equilibrium period from 5 to 10 ns were analyzed. According to the Einstein relation [71] for N particles in three-dimensional space mentioned in Equation 4.1.2-1, the diffusivity can be obtained by analyzing the slope of the linear segment of the mean square displacement (MSD) curve proportional to time interval (t).

$$D = \frac{1}{6t}\frac{1}{N}\sum_{i=1}^{N}\langle|r_i(t) - r_i(0)|^2\rangle \quad (4.1.2\text{-}1)$$

The diffusivity of CO_2 is found to be $7.95*10^{-6}$ cm^2/s, which is approximately 26.39% lower than the experimental value of $1.08*10^{-5}$ cm^2/s [72]. The previously observed stronger attraction between CO_2 and water molecules in the CO_2 solubility in water test can also explain this result. Because CO_2 molecules are more strongly confined by water molecules in simulation, their movements are slowed down, leading to a

doi:10.6342/NTU202403841

decrease in the diffusivity of CO_2 in water.

4.1.3 Heat of Dissociation of CO_2 Hydrate

For calculating the heat of dissociation of CO_2 hydrate, a 10 ns NPT simulation was performed at 283 K and 1 atm, and the trajectory in the equilibrium period from 6 to 10 ns is analyzed. According to Hess's law, the enthalpy difference between a pure sI CO_2 hydrate system (system a) and a two phases system containing CO_2 and water (system b) is calculated to obtain the heat of dissociation for CO_2 hydrate, and the initial structures of the two systems are shown in Model C1 (Figure 3.2-6).

The simulation results indicate that the heat of dissociation of CO_2 hydrate is 35.93 kJ/mol cages, which is approximately 21.60% lower than the experimental value of 45.83 kJ/mol cages [73, 74]. By the way, the cage occupancy of CO_2 hydrate in the experiment is about 0.788, while the hydrate used in our simulation has a cage occupancy of 1, but this may not be the primary cause of the discrepancy of simulation and experimental results. The main cause of the discrepancy is likely the stronger attractive force between CO_2 and water molecules in the simulation compared to reality, resulting in a lower enthalpy for system b and consequently a smaller enthalpy difference between the two systems, leading to a lower heat of dissociation of CO_2 hydrate.

doi:10.6342/NTU202403841

4.1.4 Melting Point of CO_2 Hydrate

For determining the melting point of CO_2 hydrate, several 100 ns NPT simulations were conducted at 284 K, 285 K, and 287 K under 60 atm, and the initial structures of the system are shown in Model D1 (Figure 3.2-7). As mentioned by Sloan et al. [2], the size of CO_2 molecules results in an occupancy of approximately 0.9614 in the large cages ($5^{12}6^2$ cages) of sI CO_2 hydrate and only about 0.5011 in the small cages (5^{12} cages). Therefore, the initial model is set with a small cage occupancy of 0.5 for sI CO_2 hydrate to better reflect the real situation. Because the dissociation of CO_2 hydrate is an endothermic reaction, the highest temperature at which the system's potential energy decreases is the lower limit of the melting temperature range, and the lowest temperature at which the system's potential energy increases is the upper limit of the melting temperature range. The variation in the system's potential energy during the simulations is shown in Figure 4.1.4-1.

The simulation results indicate that the melting temperature of CO_2 hydrate is between 285 K and 287 K at 60 atm, which is slightly higher than the experimental data [75] of 283 K by 2 to 4 K. As previously mentioned, this discrepancy may be due to the stronger attraction between CO_2 and H_2O molecules set in the simulation compared to reality, making the hydrate structure more resistant to decomposition, thereby raising the

doi:10.6342/NTU202403841

melting temperature compared to real world conditions.

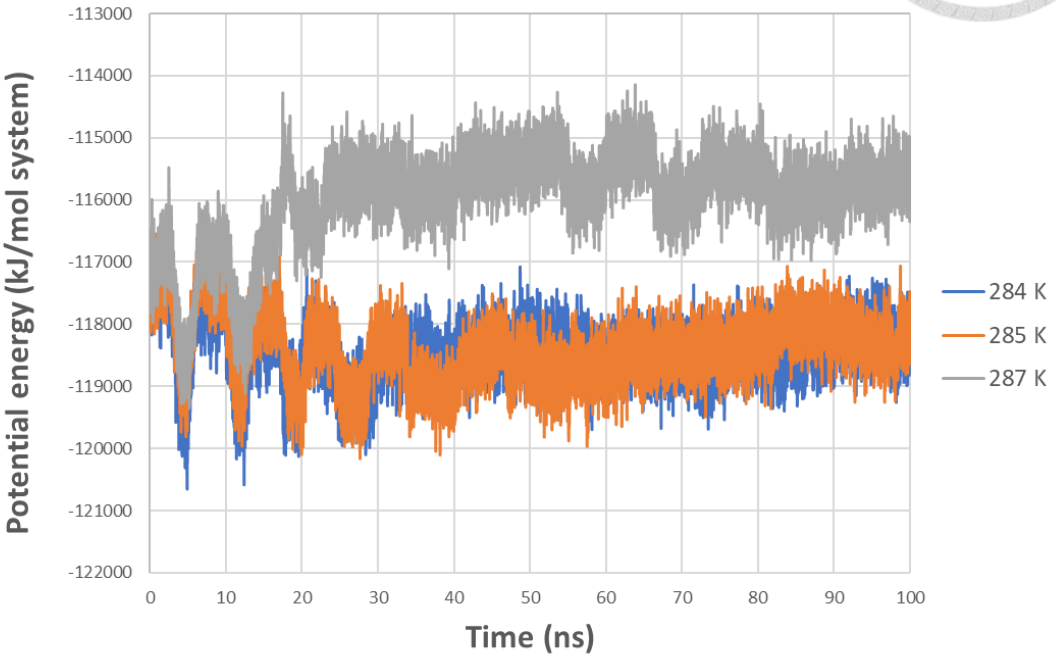

Figure 4.1.4-1 The variation in potential energy over time.

4.2 Growth of CO_2 Hydrate

4.2.1 Determination of Simulation Temperature

Before conducting CO_2 hydrate growth simulations, it is necessary to perform melting point tests to ensure that hydrate growth can be observed at the selected simulation temperature and pressure. Therefore, we conducted several 500 ns NPT simulations at a pressure of 30 bar with methionine concentrations of 0, 2, 4, and 6 methionine molecules per 736 water molecules in the initial liquid phases, and the mass

doi:10.6342/NTU202403841

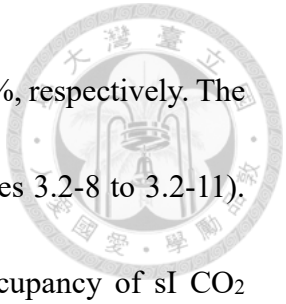

percentage concentration of methionine are 0, 2.20, 4.31, and 6.33 wt%, respectively. The initial models of each system are shown as Models D2 to D5 (Figures 3.2-8 to 3.2-11). For the reasons mentioned in the Section 4.1.4, the small cage occupancy of sI CO_2 hydrate in the systems are set to 0.5. Similar to the approach in Section 4.1.4, the changes of system potential energy at different temperatures were analyzed, and the simulation and experimental results [75] of melting temperatures are shown in Figure 4.2.1-1. The error bars represent the possible upper and lower limits of the melting point.

From the simulation results in Figure 4.2.1-1, it can be observed that as the concentration of methionine in the liquid phase increases, the melting point of CO_2 hydrate shows a slight decrease. This phenomenon is similar to the effect caused by thermodynamic inhibitors of clathrate hydrates. Although there is currently no literature directly indicating that methionine acts as a thermodynamic inhibitor for CO_2 hydrate, considering that the methionine molecules we used are in its zwitterionic form, both their amino and carboxyl groups can potentially form multiple hydrogen bonds with water molecules. This interaction can disrupt the arrangement of these water molecules and those surrounding them, and also reduce the space available for CO_2 molecules around these water molecules. Consequently, the melting point of CO_2 hydrate in systems with added methionine decreases, with the extent of the decrease being greater in systems with

doi:10.6342/NTU202403841

higher methionine concentrations in liquid phases. Additionally, we calculated the decrease in hydrate melting point with the addition of methionine based on colligative properties ($K_f = R*T_m^2/\Delta H_{fusion} = 8.314*288^2/(8.271*1000) = 83.37$ K) [76, 77], and the results are also shown in Figure 4.2.1-1. Since this calculation is only applicable to dilute solutions, it aligns more closely with the simulation result at a low methionine concentration (2.20 wt%) and shows some deviation at higher concentrations.

Based on the CO_2 hydrate melting point test results in Figure 4.2.1-1, since hydrate growth can be observed in all systems at 285 K, the subsequent simulations for CO_2 hydrate growth were conducted under the conditions of 285 K and 30 bar.

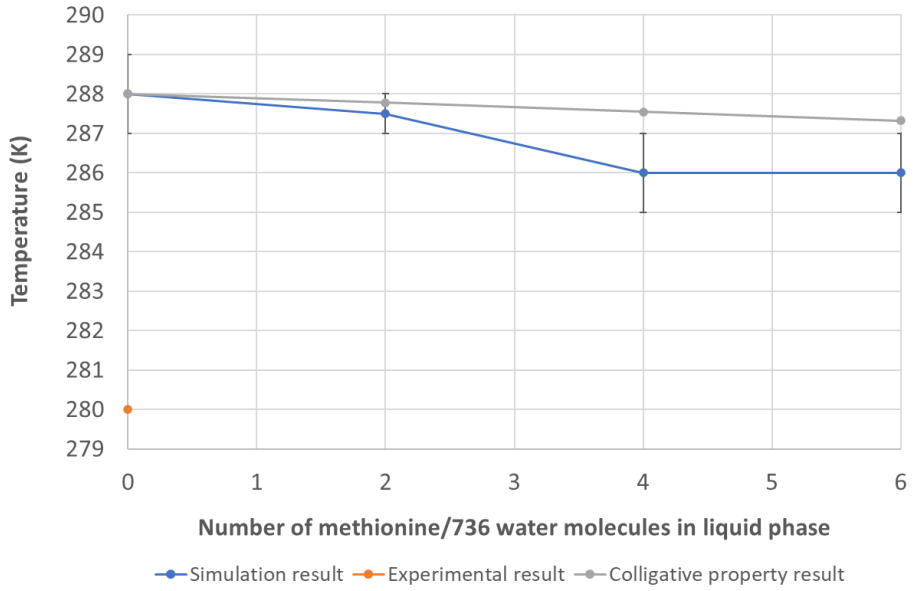

Figure 4.2.1-1 CO_2 hydrate melting point of systems with different methionine concentration. [75]

doi:10.6342/NTU202403841

4.2.2 Determination of Initial Model Structure

In the CO_2 hydrate melting point test for different methionine concentrations in Section 4.2.1, we find that the simulation time required to complete the hydrate growth is quite long (around several hundred nanoseconds). This is likely because CO_2 molecules in the gas phase must first dissolve into the liquid phase before they can participate in hydrate formation. At the given temperature and pressure conditions, CO_2 molecules do not dissolve quickly. Additionally, in the tests conducted in Section 4.2.1, we observe that methionine molecules tend to stay at the interfaces between the gas and liquid phase, as well as between the liquid phase and the hydrate. Also, Methionine is more likely to reside near the gas-liquid interface compared to the hydrate-liquid interface. Figure 4.2.2-1 illustrates this behavior with a system containing a methionine concentration of 4 methionine molecules per 736 water molecules in the liquid phase at 285 K and 30 bar. This phenomenon significantly reduces the concentration of methionine in the liquid phase, which might prevent us from seeing the expected effects at the initially preset methionine concentration. Therefore, we decide to dissolve CO_2 molecules into the liquid phase in the initial model for subsequent CO_2 hydrate growth tests to observe the complete hydrate growth process more quickly.

Since kinetic hydrate promoters may promote CO_2 hydrate growth by increasing the

doi:10.6342/NTU202403841

solubility of CO_2 molecules in the liquid phase, it is necessary to test the solubility of CO_2 molecules in solutions with different methionine concentrations. This is to ensure that this promotion effect of increasing CO_2 solubility does not occur before removing the gas phase in the initial system. We conducted several 200 ns NPT simulations at 285 K and 30 bar with methionine concentrations of 0, 2, 4, 6, and 8 methionine molecules per 1000 water molecules in the initial liquid phases, and the mass percentage concentration of methionine are 0, 1.63, 3.21, 4.74, and 6.22 wt%, respectively. The initial models of each system are shown as Models A1 to A5 (Figure 3.2-1 to 3.2-5), and the trajectories in the equilibrium period from 50 to 200 ns are analyzed. The method for analyzing CO_2 solubility is the same as that in Section 4.1.1, and the results are shown in Figure 4.2.2-2.

It can be observed that the values of CO_2 solubility in each system are very similar, and the error bars also overlap to some extent. Therefore, it can be concluded that the presence of methionine has a negligible effect on CO_2 solubility. Although there is no experimental data at this condition available for comparison, the comparison with the experimental data of Kumełan et al. [78] and Nighswander et al. [79] at 353.3 K and different pressures also shows that the addition of 6.7 wt% methionine has almost no impact on CO_2 solubility, as shown in Figure 4.2.2-3. Similar phenomenon can also be observed from the CO_2 solubility experimental data obtained by Liu et al. [39] under

doi:10.6342/NTU202403841

conditions of 293.2 K and 46 bar with the addition of 0.05 wt%, 0.1 wt%, and 0.2 wt% methionine, as shown in Figure 4.2.2-4. These results are consistent with the trends observed in our simulation results.

Therefore, from the simulation results, we can infer that removing the gas phase from the initial system should not affect our observation of methionine's promotional effect on CO_2 hydrate growth. Thus, in the subsequent CO_2 hydrate growth tests, we will dissolve CO_2 molecules into the liquid phase in the initial system.

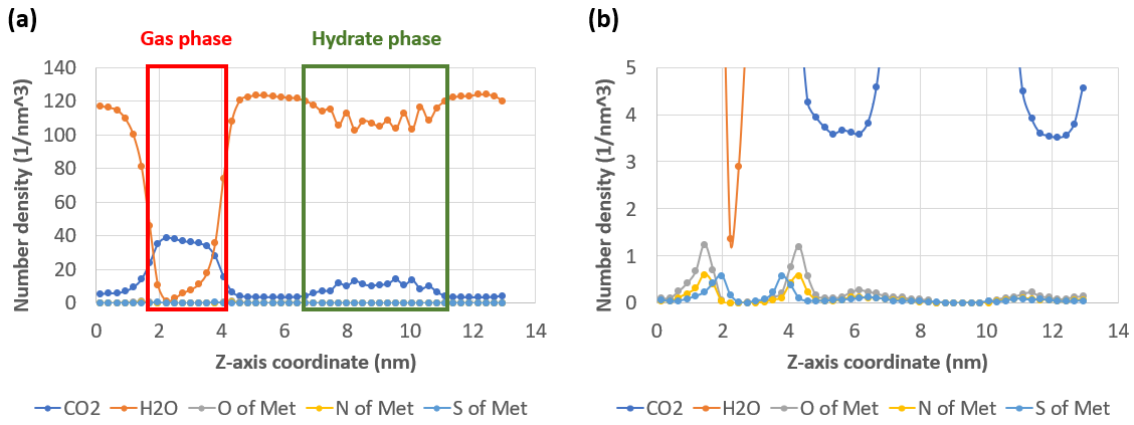

Figure 4.2.2-1 Molecules and atoms distribution in the system containing a methionine concentration of 4 methionine molecules per 736 water molecules in the liquid phase at 285 K and 30 bar. (a) Full diagram. The red box represents the CO_2 gas phase, and the green box represents the CO_2 hydrate phase. (b) Partial enlarged view of (a).

doi:10.6342/NTU202403841

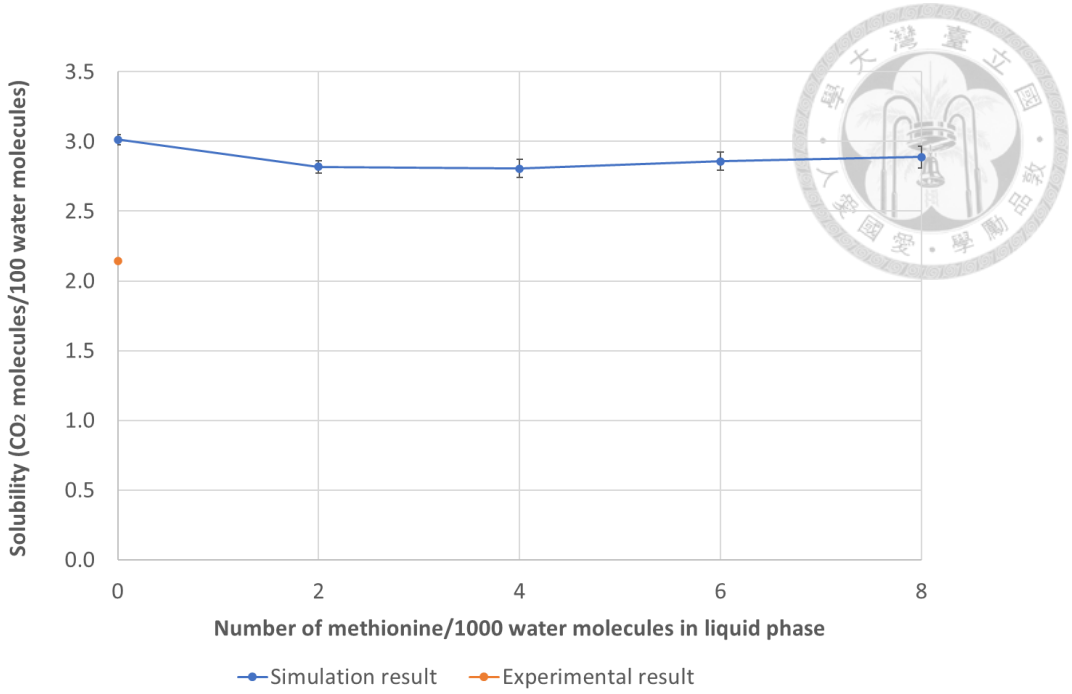

Figure 4.2.2-2 The CO_2 solubility of systems with different concentration of methionine in the liquid phase. [70]

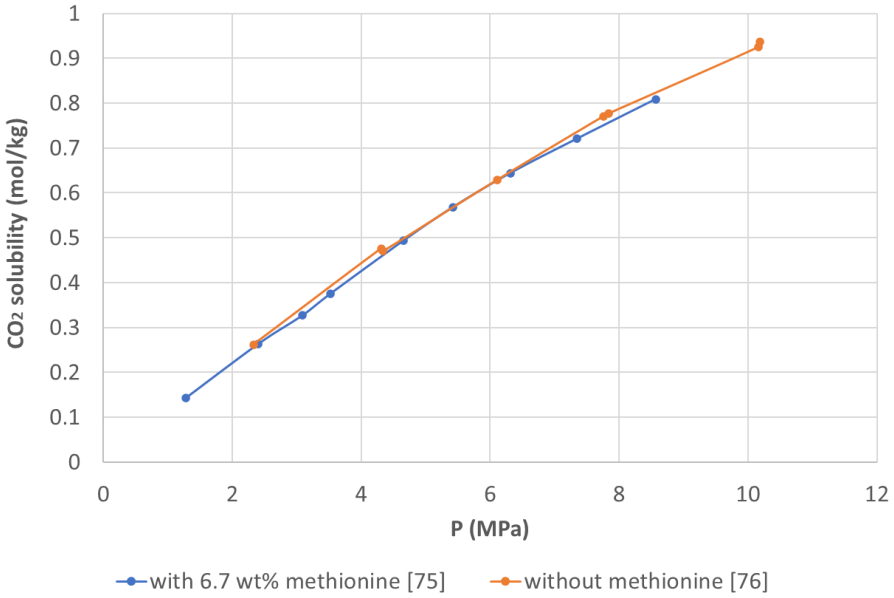

Figure 4.2.2-3 Comparison of experimental data of CO_2 solubility in systems with and without methionine at 353.3 K. [78, 79]

doi:10.6342/NTU202403841

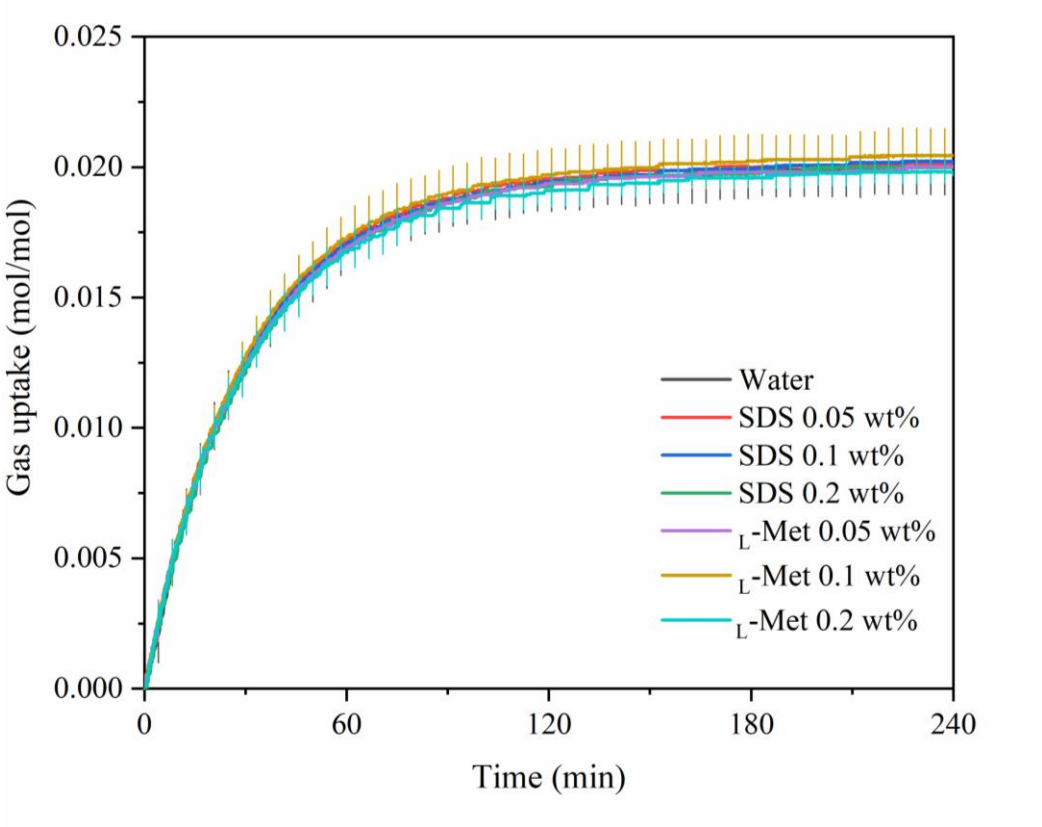

Figure 4.2.2-4 Comparison of experimental data of CO_2 solubility in systems with and without methionine at 293.2 K and 46 bar. [39]

4.2.3 Determination of CO_2 Concentration in Liquid Phase

After removing the gas phase from the initial system of the subsequent CO_2 hydrate growth test, we want to identify a CO_2 concentration in the liquid phase that allows complete utilization of CO_2 and avoids producing too little hydrate, making it difficult to compare the hydrate growth rates in subsequent tests. At 285 K and 30 bar, several 500 ns NPT simulations with CO_2 concentrations of 8, 10, 15, and 20 CO_2 molecules per 100

doi:10.6342/NTU202403841

water molecules and without methionine in the initial liquid phase were conducted to observe the growth of CO_2 hydrate. The initial model, exemplified by the system with a CO_2 concentration of 10 CO_2 molecules per 100 water molecules, is shown as Model E1 (Figure 3.2-12).

For the CO_2 concentration limits in this test, the lower limit of 8 is chosen considering the solubility of CO_2 in water at 285 K and 30 bar, which is approximately 3 CO_2 molecules per 100 water molecules. Hydrate growth only occurs when the gas in the liquid phase reaches supersaturation, thus we chose a value of 8. The upper limit of 20 is selected based on the value of perfect crystalline sI CO_2 hydrate, calculated as 100*8/46 = 17.39, with 20 chosen as a slightly higher upper limit.

Snapshots of hydrate growth at 500 ns for systems with different CO_2 concentrations in the liquid phase are shown in Figure 4.2.3-1. Only hydrogen bonds between water molecules are displayed to clearly illustrate the hydrate. The quantified hydrate growth via the F4 order parameter is shown in Figure 4.2.3-2. From Figure 4.2.3-1 and 4.2.3-2, it can be observed that the hydrate quantity at a concentration of 8 CO_2 molecules per 100 water molecules is relatively low. Although the concentration of 20 CO_2 molecules per 100 water molecules yields a higher hydrate quantity, it takes approximately 380 ns to reach its maximum hydrate content, which is too slow. Therefore, the concentrations of

doi:10.6342/NTU202403841

10 and 15 CO_2 molecules per 100 water molecules are selected for subsequent tests.

To determine at which CO_2 concentration in liquid phase we are more likely to observe faster hydrate growth in systems with methionine compared to systems without methionine, we conducted several 500 ns NPT simulations with CO_2 concentrations of 10 and 15 CO_2 molecules per 100 water molecules. For each CO_2 concentration system, we vary the methionine concentration in the liquid phase, adding 0, 2, 4, and 6 methionine molecules to the liquid phases on both sides of the hydrate in the initial models, and the mass percentage concentration of methionine after excluding CO_2 are 0, 2.20, 4.31, and 6.33 wt%, respectively. For example, in systems with a CO_2 concentration of 10 CO_2 molecules per 100 water molecules, the initial systems are shown as Model E1, E4, E5, and E6 (Figure 3.2-12, 3.2-15, 3.2-16, and 3.2-17).

Figure 4.2.3-3 shows the results of F4 order parameter for CO_2 concentrations of 10 and 15 CO_2 molecules per 100 water molecules. The comparison of the slopes of trend lines for both concentrations is shown in Table 4.2.3-1. The slopes of the F4 order parameter trend lines are calculated using the initial 20 ns data for the concentration of 10 CO_2 molecules per 100 water molecules, and using the initial 30 ns data for the concentration of 15 CO_2 molecules per 100 water molecules.

From Table 4.2.3-1, it can be observed that the trend line slopes for the systems with

doi:10.6342/NTU202403841

methionine is higher than the slope for system without methionine at a CO_2 concentration of 10 CO_2 molecules per 100 water molecules, whereas at a CO_2 concentration of 15 CO_2 molecules per 100 water molecules, the result is reversed. Based on this observation, it is inferred that the promotional effect of methionine on CO_2 hydrate growth is more likely to be observed at a CO_2 concentration of 10 CO_2 molecules per 100 water molecules. Therefore, this concentration is chosen for further simulations of CO_2 hydrate growth.

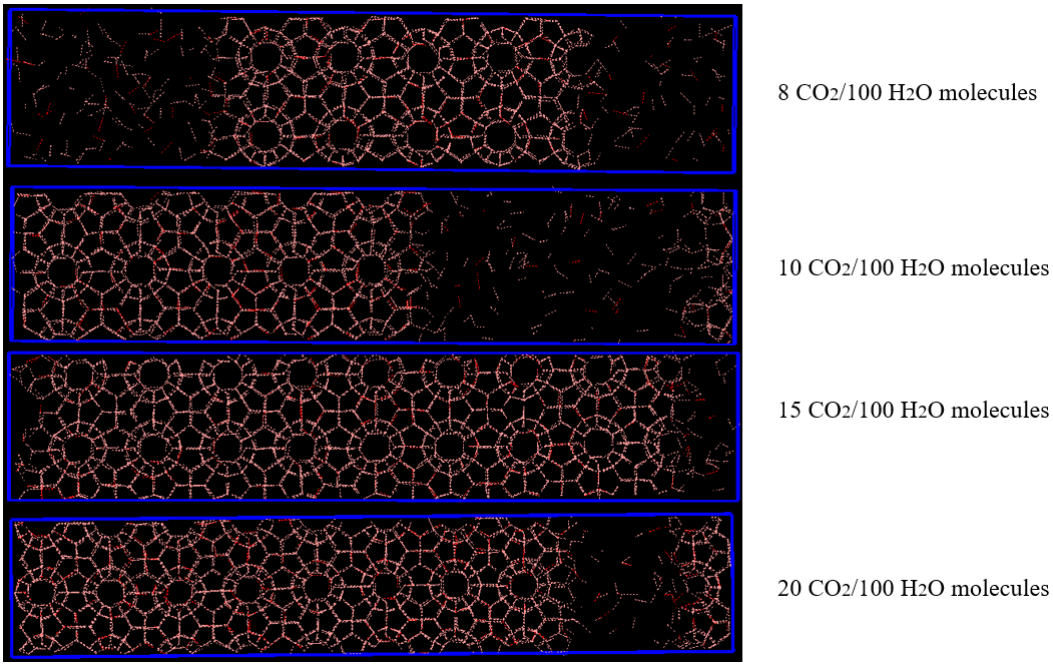

Figure 4.2.3-1 Snapshots of hydrate growth for CO_2 concentration test of systems without methionine.

doi:10.6342/NTU202403841

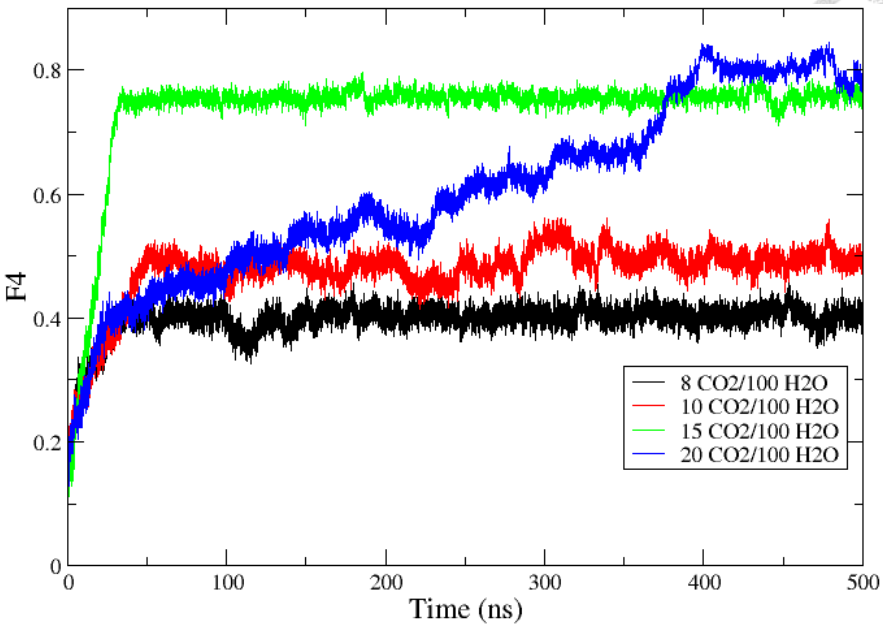

Figure 4.2.3-2 F4 order parameter for CO_2 concentration test of systems without methionine.

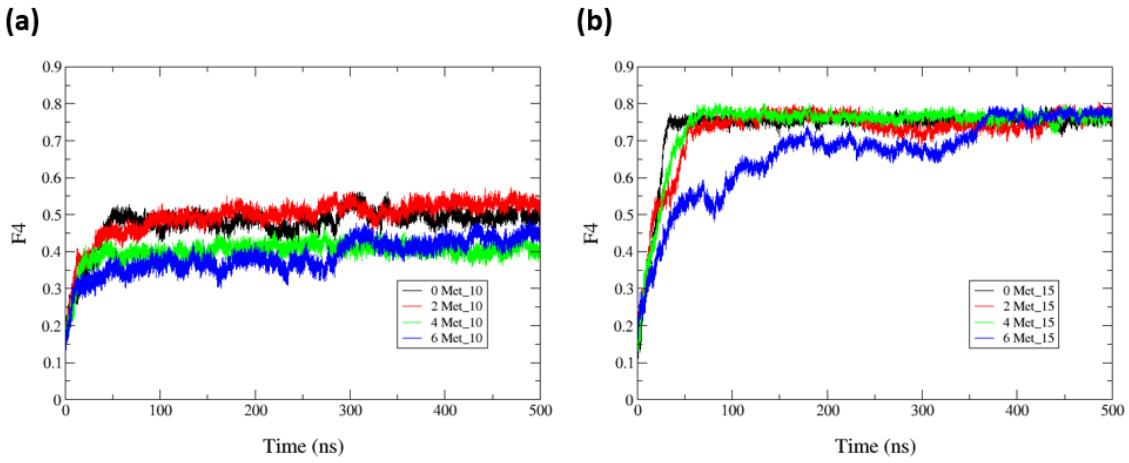

Figure 4.2.3-3 F4 order parameter for systems of different CO_2 concentrations. (a) 10 CO_2 molecules per 100 water molecules. (b) 15 CO_2 molecules per 100 water molecules.

doi:10.6342/NTU202403841

Table 4.2.3-1 F4 order parameter trend line slopes for both CO_2 concentrations.

Number of methionine	F4 OP trend line slope (conc.: 10 CO_2/100 H_2O)	F4 OP trend line slope (conc.: 15 CO_2/100 H_2O)
0	0.0071	0.0193
2	0.0114	0.0136
4	0.0112	0.0136
6	0.0083	0.0081

4.2.4 Formal Test of CO_2 Hydrate Growth

For the CO_2 hydrate growth test, we selected six different concentrations of methionine in the liquid phase: 0, 1, 2, 4, 8, and 12 methionine molecules per 1472 water molecules, and the mass percentage concentration of methionine after excluding CO_2 are 0, 0.56, 1.11, 2.20, 4.31, and 6.33 wt%, respectively. The initial models of the systems are shown in Model E1 to E6 (Figure 3.2-12 to 3.2-17). We conducted 10 sets of 20 ns NPT simulations at 285 K and 30 bar for each system. For each methionine concentration, the trend line slopes of the F4 order parameter are calculated from different time segments and averaged over the 10 simulations, as shown in Figure 4.2.4-1. Similarly, the trend line slopes of the hydrate volume variation are calculated from different time segments and averaged over the 10 simulations, as shown in Figure 4.2.4-2. The hydrate volume referred to here is calculated using the method mentioned in Section 3.4.2. After

doi:10.6342/NTU202403841

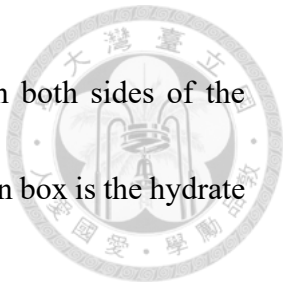

determining the interfaces between the hydrate and liquid phase on both sides of the hydrate, the volume between these two interfaces within the simulation box is the hydrate volume.

From Figure 4.2.4-1, it can be observed that when the methionine concentration in the liquid phase is 1 methionine molecule per 1472 water molecules (0.56 wt%), the average trend line slope of the F4 order parameter is the highest, regardless of the time segment analyzed within 20 ns. This suggests that at this concentration, methionine may have a promoting effect on hydrate growth. Additionally, Figure 4.2.4-2 also reveals a similar trend to Figure 4.2.4-1, further confirming the hypothesis regarding Figure 4.2.4-1 analysis that a specific low concentration of methionine in liquid phase can promote CO_2 hydrate growth. Moreover, we observed that if methionine becomes trapped on that side of the hydrate rather than just staying near the hydrate-liquid interface, the hydrate growth on that side becomes significantly slower.

doi:10.6342/NTU202403841

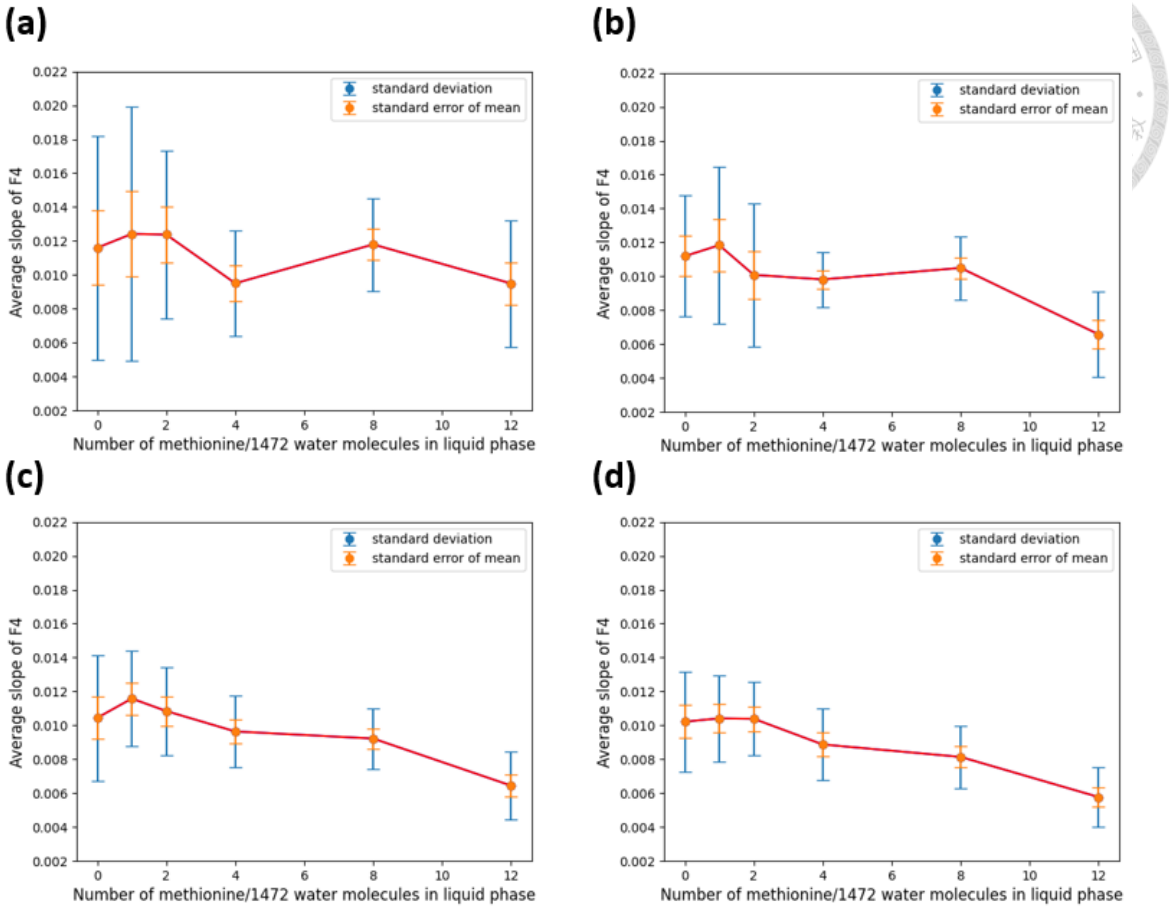

Figure 4.2.4-1 Average slope of F4 order parameter trend line versus number of methionine per 1472 water molecules in liquid phase. (a) 0~5 ns. (b) 0~10 ns. (c) 0~15 ns. (d) 0~20 ns.

doi:10.6342/NTU202403841

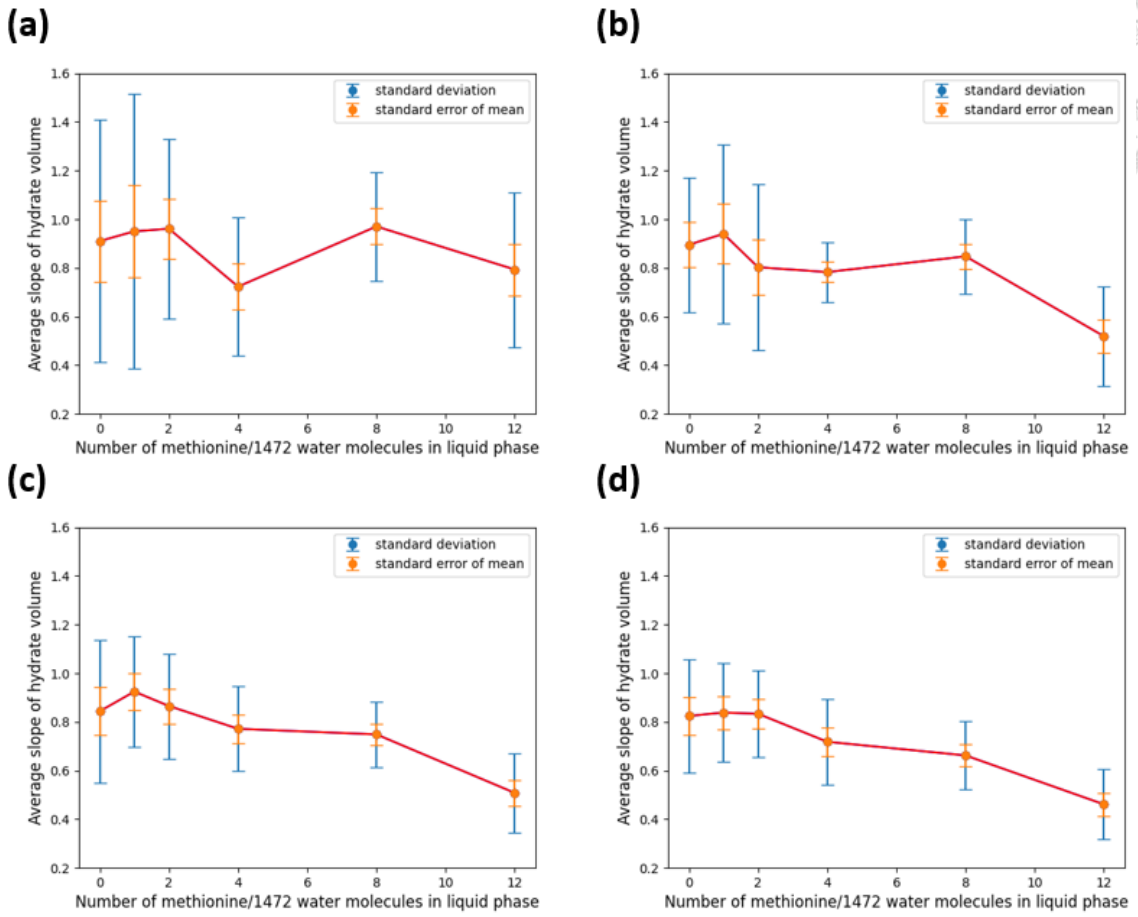

Figure 4.2.4-2 Average slope of hydrate volume trend line versus number of methionine per 1472 water molecules in liquid phase. (a) 0~5 ns. (b) 0~10 ns. (c) 0~15 ns. (d) 0~20 ns.

4.3 Effects of Methionine on CO_2 Hydrate Growth

4.3.1 Amount of Methionine around CO_2 Hydrate

We analyzed a total of 60 simulations from the CO_2 hydrate growth test, encompassing all methionine concentrations in the liquid phase. Each simulation contains

doi:10.6342/NTU202403841

two interfaces between the hydrate and the liquid phase, resulting in a total of 120 interfaces. For each interface, we calculated the average number of sulfur and nitrogen atoms of methionine within a 1.0 nm range from the hydrate-liquid interface over 20 ns. The selected space is shown in Figure 4.3.1-1. Simultaneously, we computed the trend line slope of the hydrate volume from the center of the initial hydrate seed to the interface. These data were then grouped based on the average number of sulfur and nitrogen atoms of methionine within a 1.0 nm range from the hydrate-liquid interface over 20 ns, and we calculated the mean and standard deviation for each group. The method for grouping involved subtracting the minimum value from the maximum value of the calculated average number of atoms, and then dividing by the square root of the number of samples. This provided the bin width for categorization. The resulting relationship is shown in Figure 4.3.1-2.

Figure 4.3.1-2 depicts the relationship between the mean of trend line slopes of the hydrate volume growth and the average number of sulfur and nitrogen atoms of methionine within a 1.0 nm range from the hydrate-liquid interface over 20 ns. It can be observed that when there is an average of about 0.4 sulfur atoms around the hydrate-liquid interface, the hydrate volume growth rate is slightly higher compared to samples without methionine and with more methionine near the hydrate-liquid interface.

doi:10.6342/NTU202403841

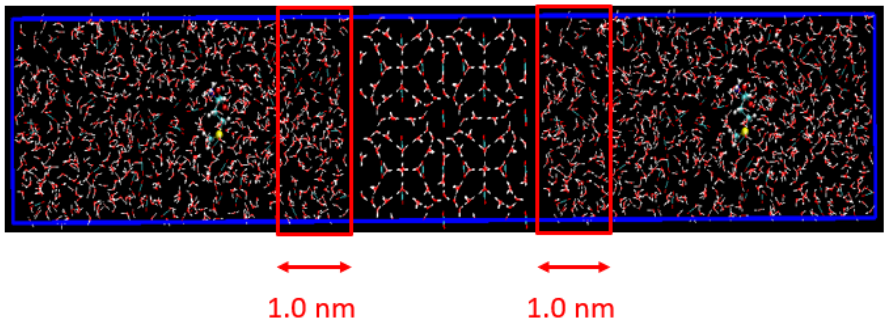

Figure 4.3.1-1 Schematic diagram for selected space in calculation of the average number of sulfur and nitrogen atoms of methionine.

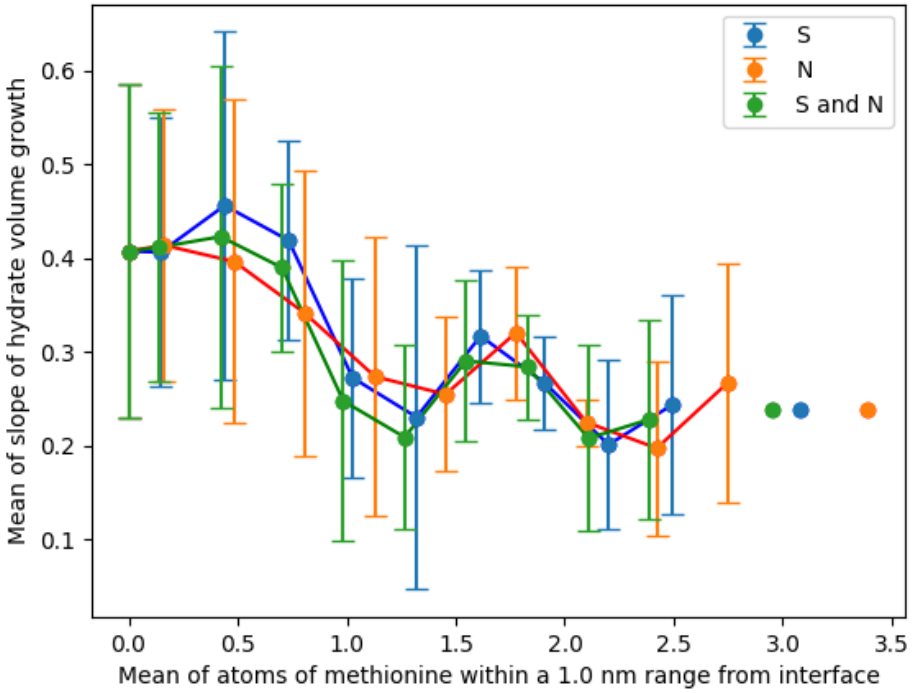

Figure 4.3.1-2 Mean of slope of hydrate volume growth trend line versus average number of sulfur and nitrogen atoms of methionine within a 1.0 nm range from the hydrate-liquid interface over 20 ns. (The S and N represent the sulfur and nitrogen atoms of methionine molecule respectively.)

doi:10.6342/NTU202403841

4.3.2 Diffusivity

For the diffusivity of CO_2 in methionine solution test, we selected six different concentrations of methionine in the liquid phase: 0, 1, 2, 4, 6, and 8 methionine molecules per 1000 water molecules, and the mass percentage concentration of methionine after excluding CO_2 are 0, 0.82, 1.63, 3.21, 4.74, and 6.22 wt%, respectively. The initial models of each system are shown as Model B2 to B7. A 100 ns NPT simulation was conducted at 285 K and 30 bar for each system, and the trajectory in the equilibrium period from 90 to 100 ns was analyzed. The results of calculating the diffusivity of the three types of molecules using the same method as in Section 4.1.2 are shown in Figure 4.3.2-1.

From the results, it can be observed that the diffusivity of water molecules generally decreases as the concentration of methionine increases. This is likely because methionine forms hydrogen bonds with water molecules. Since methionine molecules are heavier, the diffusivity of water molecules bonded to methionine naturally decreases, leading to an overall reduction in the average diffusivity of water molecules. The diffusivity of methionine molecules also shows a similar trend to that of water molecules. In contrast, the diffusivity of CO_2 molecules generally increases with the increasing concentration of methionine. This might be one of the reasons for the promotion effect of methionine on CO_2 hydrate growth. However, since the diffusivity of water molecules decreases with

doi:10.6342/NTU202403841

increasing methionine concentration, this synergistic effect could be why we observed a promotional effect only in systems with lower methionine concentrations in the initial liquid phase, as mentioned in Section 4.2.4.

Additionally, as mentioned in Section 4.2.2, methionine tends to stay near the hydrate-liquid interface rather than in the liquid phase, thus having a greater impact on the molecules near the interface. Therefore, the effect of methionine concentration on the diffusivity of CO_2 and water molecules discussed here could explain why the promotional effect on CO_2 hydrate growth is observed only when there is a very small amount of methionine around the hydrate-liquid interface, as mentioned in Section 4.3.1.

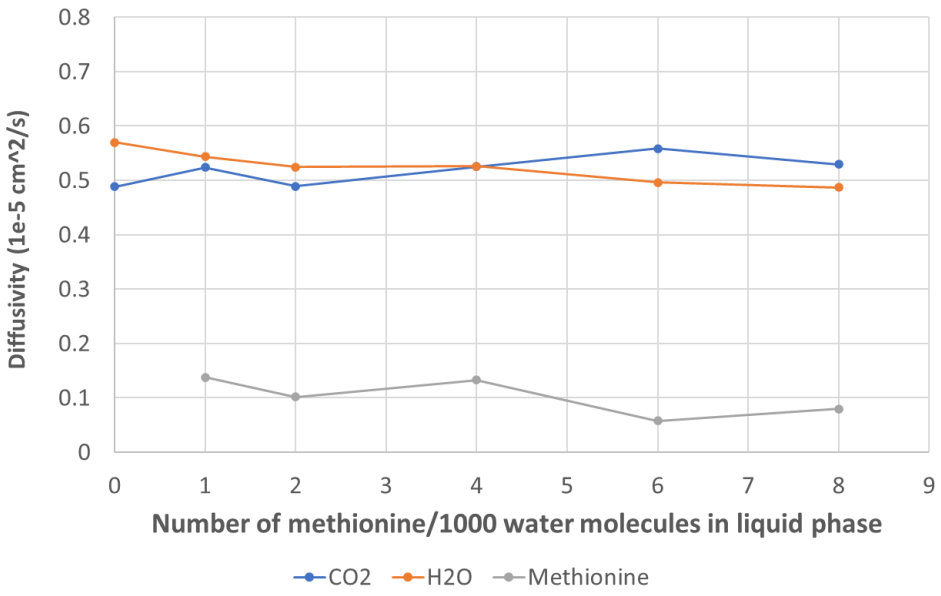

Figure 4.3.2-1 The diffusivity of the three types of molecules for systems with different concentration of methionine in the liquid phase at 285 K and 30 bar.

doi:10.6342/NTU202403841

4.3.3 Radial Distribution Function (RDF)

Since we know that methionine tends to reside near the hydrate-liquid interface, if the presence of methionine can cause CO_2 molecules around it to become more concentrated, it may help increase the CO_2 concentration around the hydrate-liquid interface, which would be more conducive to the growth of CO_2 hydrate. Therefore, we analyzed the radial distribution function (RDF) [80] of the carbon atoms of CO_2 molecules to verify this hypothesis. The trajectories analyzed here were from the diffusivity test in Section 4.3.2. These RDF values were categorized based on the shortest distance between the two atoms of each pair and the nitrogen atoms and the terminal carbon atoms (CS3J in Figure 3.3-1) of methionine molecules. This approach yields RDF curves related to the distances from methionine. The results are shown in Figure 4.3.3-1 and Figure 4.3.3-2. The left side of these figures displays the original RDF curves, while the right side shows the re-normalized (rescaled) RDF curves. The purpose of re-normalization is to ensure that each RDF curve converges to a value of 1 at long distances between pair atoms, allowing for a more equitable comparison of the curves.

From these results, it can be observed that CO_2 molecules tend to aggregate more as their distance from the nitrogen atoms and terminal carbon atoms in methionine increases. This indicates that methionine does not have the capability to facilitate the aggregation of

doi:10.6342/NTU202403841

CO_2 and water molecules around it. Therefore, this is unlikely to be the reason why methionine promotes CO_2 hydrate growth.

doi:10.6342/NTU202403841

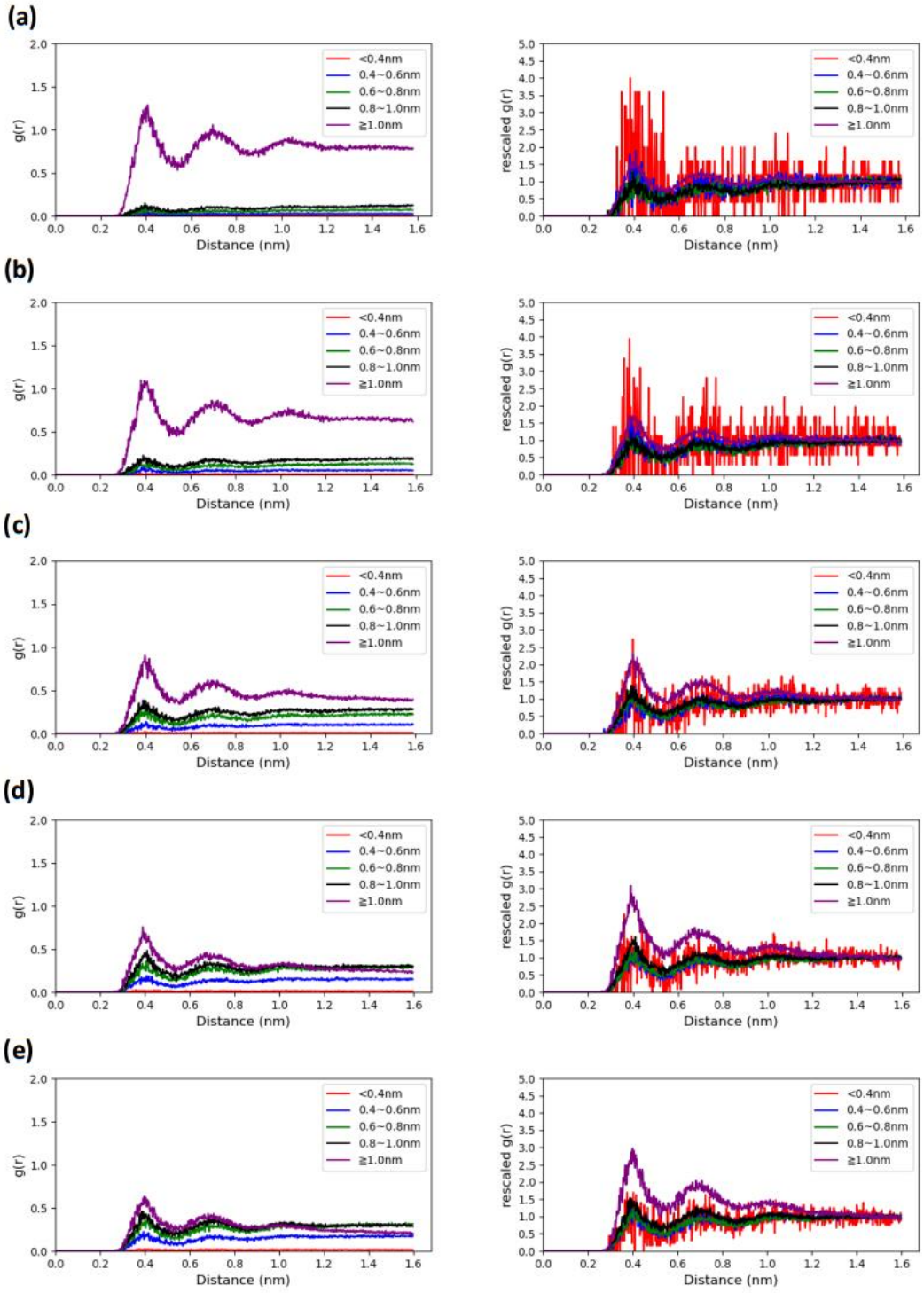

Figure 4.3.3-1 RDF of carbon atoms of CO_2 related to the shortest distance between the pair and the nitrogen atom of methionine (left: RDF, right: rescaled RDF). (a) 1 Met system. (b) 2 Met system. (c) 4 Met system. (d) 6 Met system. (e) 8 Met system.

doi:10.6342/NTU202403841

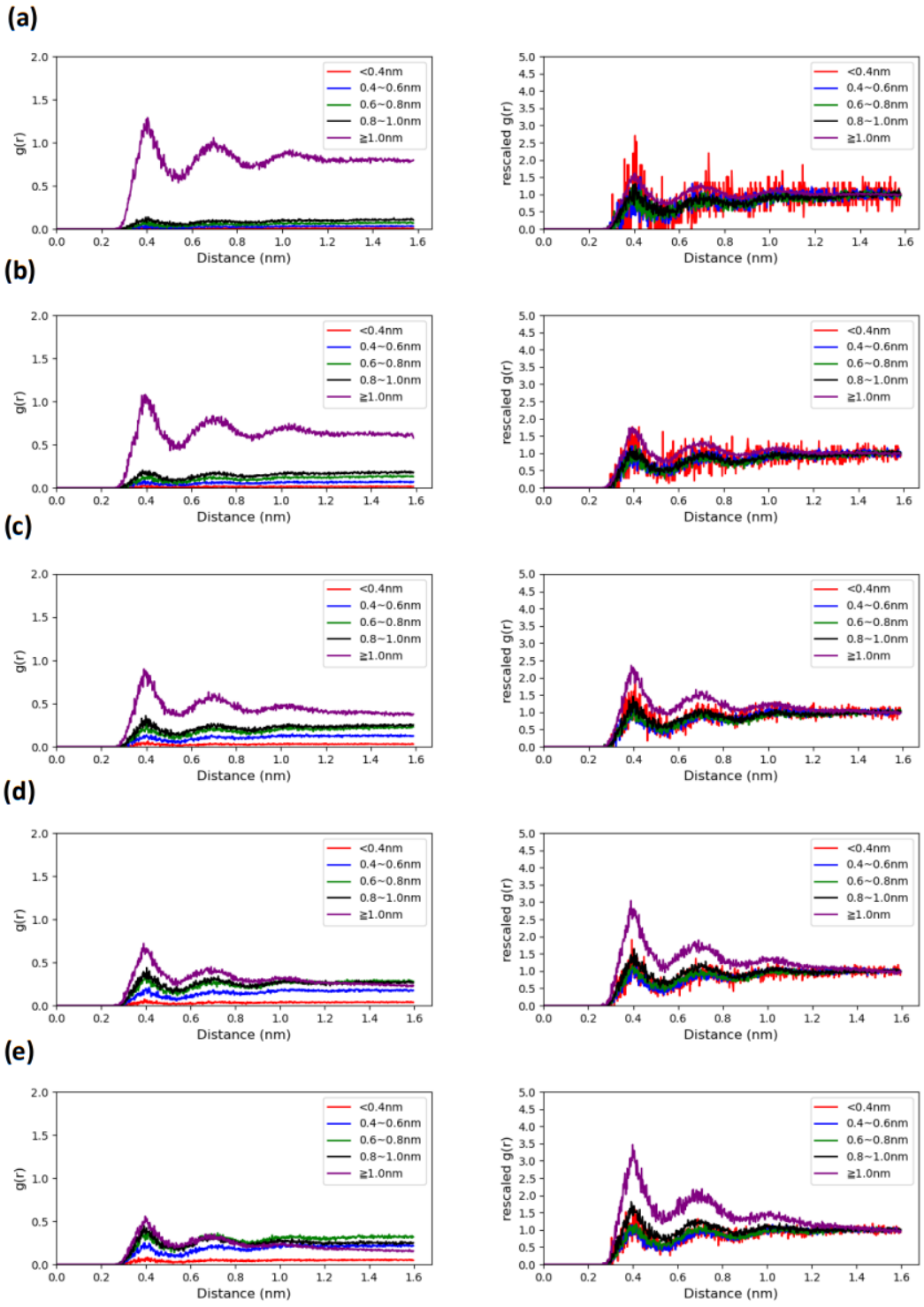

Figure 4.3.3-2 RDF of carbon atoms of CO_2 related to the shortest distance between the pair and the terminal carbon atom of methionine (left: RDF, right: rescaled RDF). (a) 1 Met system. (b) 2 Met system. (c) 4 Met system. (d) 6 Met system. (e) 8 Met system.

doi:10.6342/NTU202403841

4.4 Nucleation of CO_2 Hydrate

4.4.1 Determination of CO_2 Concentration in Liquid Phase

In the tests of CO_2 hydrate nucleation, initially, the intention was to maintain the CO_2 concentration in the liquid phase at 10 CO_2 molecules per 100 water molecules, as used in the previous CO_2 hydrate growth tests. However, after multiple simulations with a duration of 500 ns, it was observed that nucleation could not occur even when cooling to 250 K at 30 bar. Consequently, the decision was made to increase the CO_2 concentration in the liquid phase. The candidate concentrations were 15 and 17.39 (the value for perfect sI CO_2 hydrate) CO_2 molecules per 100 water molecules in the liquid phase. The F4 order parameter results from the tests are depicted in Figure 4.4.1-1.

From Figure 4.4.1-1, it is evident that the nucleation time for CO_2 concentration of 15 CO_2 molecules per 100 water molecules is shorter than that for 17.39 CO_2 molecules per 100 water molecules at the condition of 260 K and 30 bar. Therefore, the final decision was to proceed with simulations for CO_2 hydrate nucleation in single-phase system with a concentration of 15 CO_2 molecules per 100 water molecules at 260 K and 30 bar.

doi:10.6342/NTU202403841

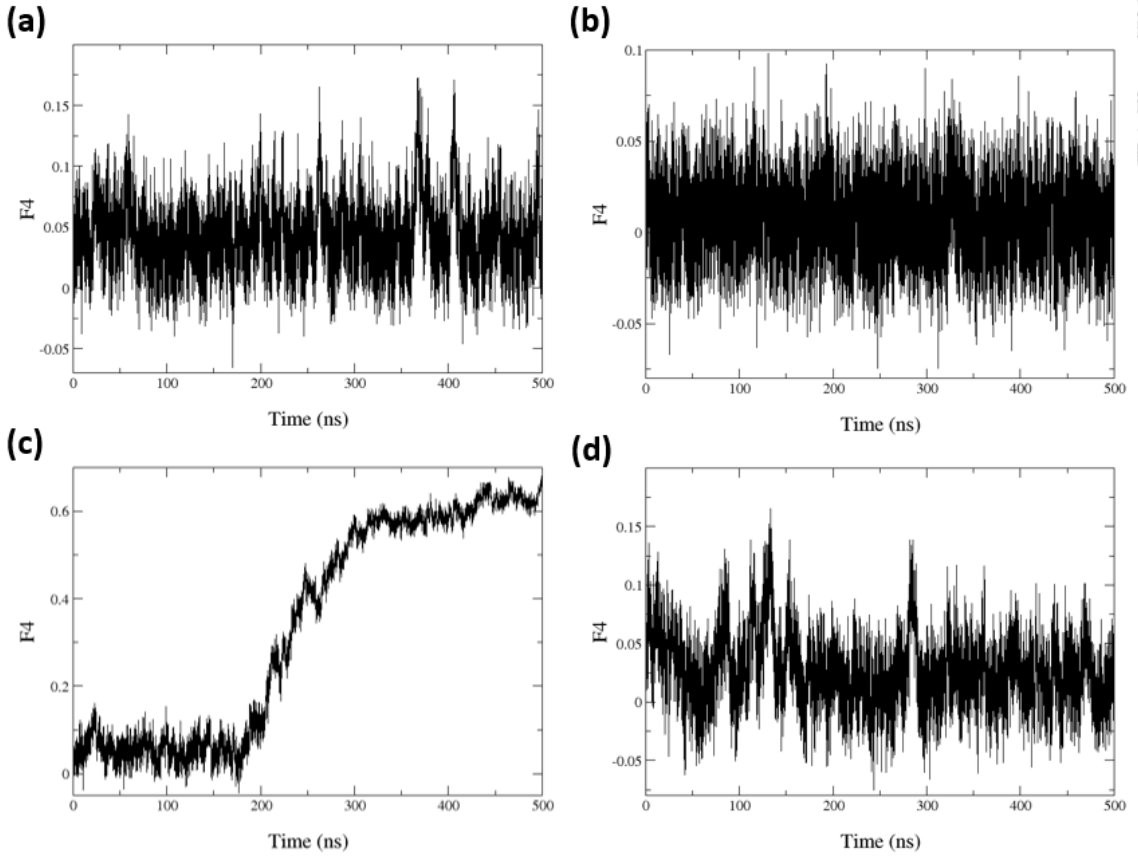

Figure 4.4.1-1 F4 order parameter for CO_2 concentration of 15 and 17.39 CO_2 molecules per 100 water molecules in the liquid phase. (a) CO_2 concentration: 15 (265 K). (b) CO_2 concentration: 17.39 (265 K). (c) CO_2 concentration: 15 (260 K). (d) CO_2 concentration: 17.39 (260 K).

4.4.2 Nucleation of CO_2 Hydrate in Single-Phase Systems

For the CO_2 hydrate nucleation in single-phase systems test, we selected two different concentrations of methionine in the liquid phase: 0 and 1 methionine molecule per 1000 water molecules, and the mass percentage concentration of methionine after

doi:10.6342/NTU202403841

excluding CO_2 are 0 and 0.82 wt%, respectively. The initial models of the systems are shown in Model F1 and Model F2. We conducted 15 sets of 500 ns NPT simulations at 260 K and 30 bar for both systems.

The results of the two systems fitted and calculated using the mean first-passage time (MFPT) method [66] are shown in Figure 4.4.2-1 and Table 4.4.2-1. The τ_J is induction time, the Z is Zeldovich factor, the n* is critical cluster size, the G is growth rate, and the J is nucleation rate in Table 4.4.2-1. The distribution of induction times for each simulation, determined based on the calculated critical cluster size (n*), is shown in Figure 4.4.2-2. For simulations that did not successfully nucleate within 500 ns, the induction time was recorded as 500 ns.

In Figure 4.4.2-1, the green curve is fitted to the original MFPT curve using Equation (3.4.4-2), and the red curve is fitted using Equation (3.4.4-3). This indicates that in our simulations, the hydrate growth rate was not fast enough, necessitating the use of Equation (3.4.4-3) to obtain more accurate nucleation-related parameters. Table 4.4.2-1 shows that at 260 K and 30 bar, there is no significant difference in the hydrate nucleation rate and hydrate growth rate between the two systems. However, this might be due to the small sample size in our test.

The sample size is limited to 15 because Figure 4.4.2-2 shows that one-third of the

doi:10.6342/NTU202403841

simulations in both systems have induction times in the 0 to 50 ns range. Such rapid induction times could indicate the occurrence of spinodal decomposition [81], which is not the nucleation phenomenon we intend to observe. To avoid concerns about the occurrence of spinodal decomposition in simulations with very short induction times, we decided to increase the simulation temperature from 260 K to 262 K to reduce the subcooling temperature during nucleation.

After the adjustment of simulation temperature, we conducted 50 sets of 500 ns NPT simulations at 262 K and 30 bar for both systems. The results of the two systems fitted and calculated using the mean first-passage time (MFPT) method [66] are shown in Figure 4.4.2-3 and Table 4.4.2-2. The distribution of induction times for each simulation, determined based on the calculated critical cluster size (n*), is shown in Figure 4.4.2-4.

From Figure 4.4.2-4, it can be observed that the proportion of simulations with induction times in the 0 to 50 ns range has significantly decreased in both systems, indicating that the chosen temperature of 262 K meets our requirements. Additionally, Table 4.4.2-2 shows that although no promotional effect of methionine on the CO_2 hydrate nucleation rate is observed under our simulation conditions, it enhances the hydrate growth rate, with an increase of approximately 36.61%. Moreover, the methionine concentration in the initial liquid phase of this system (0.82 wt%) is quite close to the

doi:10.6342/NTU202403841

concentration (0.56 wt%) found to have a promoting effect in the CO_2 hydrate growth in Section 4.2.4, demonstrating consistency.

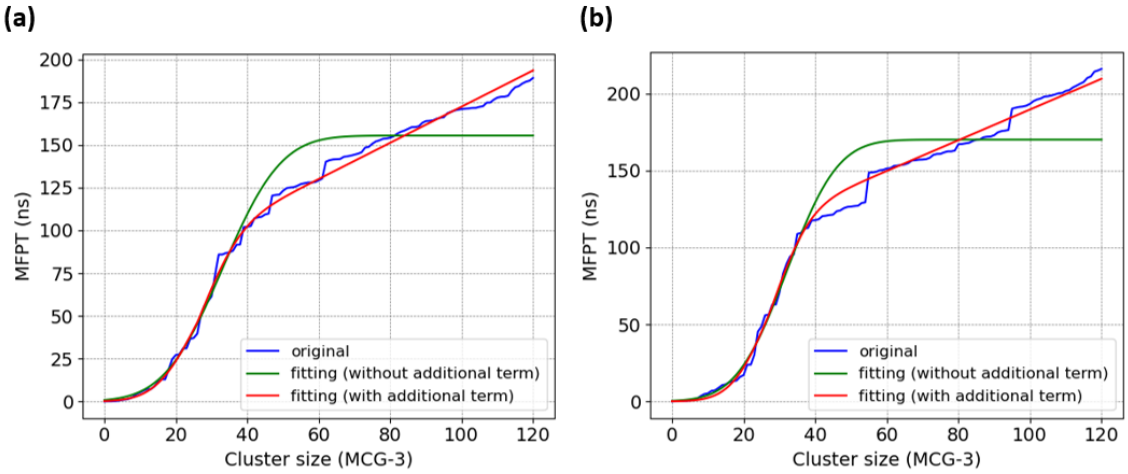

Figure 4.4.2-1 MFPT curve fitting results for CO_2 hydrate nucleation in single-phase systems at 260 K and 30 bar (15 sets of simulations for each system). (a) 0 Met system. (b) 1 Met system.

doi:10.6342/NTU202403841

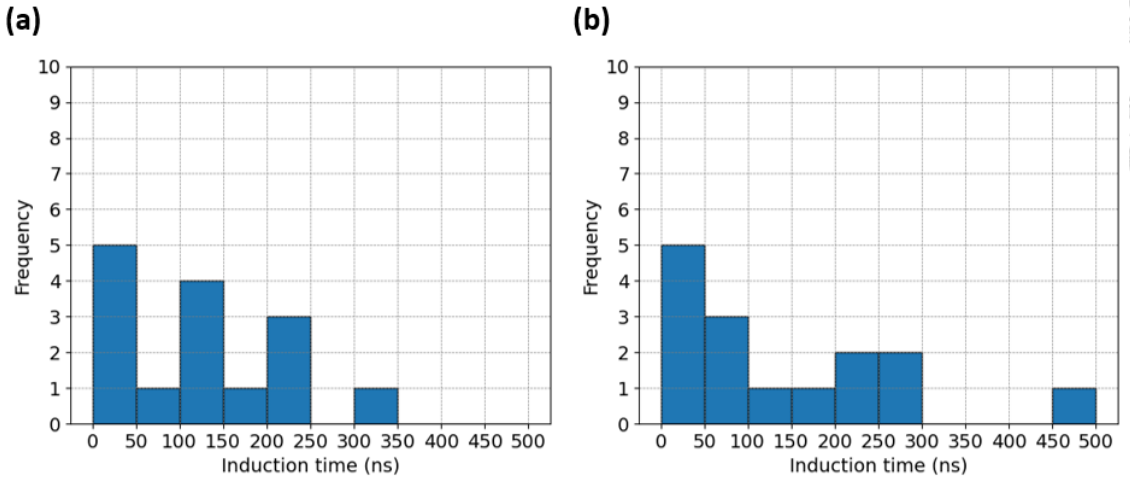

Figure 4.4.2-2 Distribution of induction time for CO_2 hydrate nucleation in single-phase systems at 260 K and 30 bar (15 sets of simulations for each system). (a) 0 Met system. (b) 1 Met system.

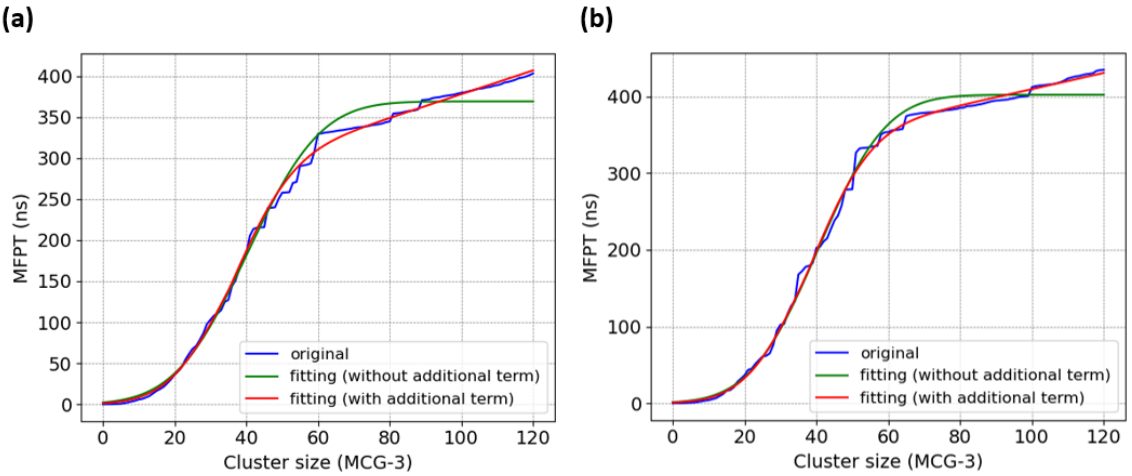

Figure 4.4.2-3 MFPT curve fitting results for CO_2 hydrate nucleation in single-phase systems at 262 K and 30 bar (50 sets of simulations for each system). (a) 0 Met system. (b) 1 Met system.

doi:10.6342/NTU202403841

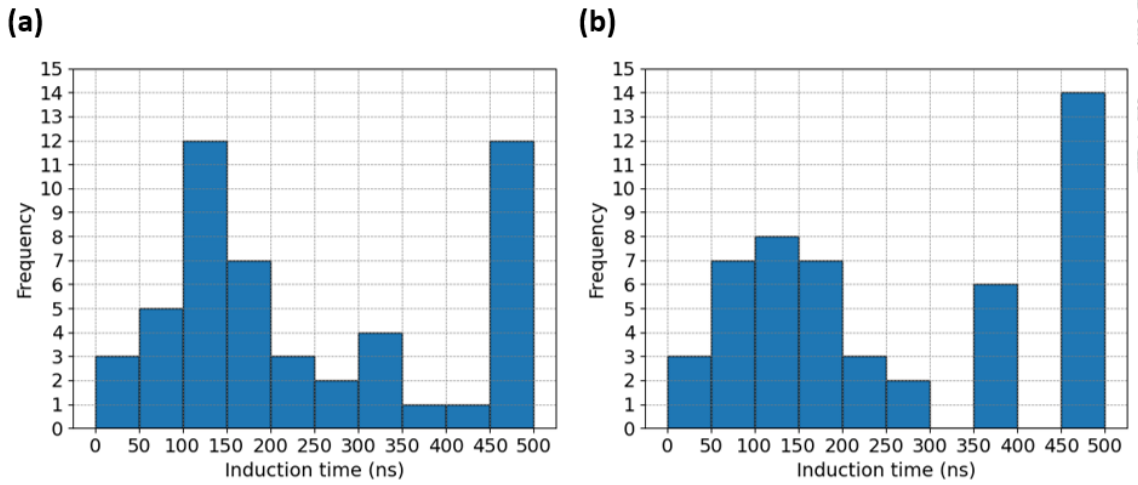

Figure 4.4.2-4 Distribution of induction time for CO_2 hydrate nucleation in single-phase systems at 262 K and 30 bar (50 sets of simulations for each system). (a) 0 Met system. (b) 1 Met system.

Table 4.4.2-1 MFPT curve fitting results for CO_2 hydrate nucleation in single-phase systems at 260 K and 30 bar. Each system has 15 simulation sets, and the values in parentheses are the standard errors.

System	τ_J (ns)	Z	n^* (MCG-3)	$J \times 10^5$ ($nm^{-3}ns^{-1}$)	G (MCG-3/ns)
0 Met	94.340 (3.293)	0.04305 (0.00138)	26.2 (0.4)	25.9403 (0.90539)	0.945 (0.056)
1 Met	117.226 (3.308)	0.04724 (0.00135)	27.5 (0.3)	20.7558 (0.58574)	1.002 (0.065)

doi:10.6342/NTU202403841

Table 4.4.2-2 MFPT curve fitting results for CO_2 hydrate nucleation in single-phase systems at 262 K and 30 bar. Each system has 50 simulation sets, and the values in parentheses are the standard errors.

System	τ_J (ns)	Z	n^* (MCG-3)	$J \times 10^5$ ($nm^{-3}ns^{-1}$)	G (MCG-3/ns)
0 Met	284.406 (5.136)	0.02963 (0.00048)	35.4 (0.3)	8.60464 (0.15540)	0.691 (0.039)
1 Met	343.404 (5.222)	0.02960 (0.00043)	37.6 (0.3)	7.08533 (0.10774)	0.944 (0.078)

4.4.3 Nucleation of CO_2 Hydrate in Two-Phase Systems

In addition to the single-phase systems, we also conducted CO_2 hydrate nucleation tests with two-phase systems. The reason we conduct tests on two-phase systems is that hydrate nucleation experiments in reality also involve two-phase systems [39]. Therefore, using two-phase systems in simulations might better reflect real-world conditions. For the CO_2 hydrate nucleation in two-phase systems test, we selected two different concentrations of methionine in the liquid phase: 0 and 1 methionine molecule per 1242 water molecules, and the mass percentage concentration of methionine are 0 and 0.66 wt%, respectively. The initial models of the systems are shown in Model F3 and Model F4 (Figure 3.2-18 and Figure 3.2-19). We conducted 20 sets of 500 ns NPT simulations at 262 K and 500 bar for both systems. The reason for changing the pressure to 500 bar

doi:10.6342/NTU202403841

was to allow CO_2 to dissolve more quickly into the liquid phase to achieve the supersaturated state required for nucleation.

The results of the two systems fitted and calculated using the mean first-passage time (MFPT) method [66] are shown in Figure 4.4.3-1 and Table 4.4.3-1. The τ_J is induction time, the Z is Zeldovich factor, the n* is critical cluster size, the G is growth rate, and the J is nucleation rate in Table 4.4.3-1. In Figure 4.4.3-1, the green curve is fitted to the original MFPT curve using Equation (3.4.4-2), and the red curve is fitted using Equation (3.4.4-3). This indicates that in our simulations, the hydrate growth rate was not fast enough, necessitating the use of Equation (3.4.4-3) to obtain more accurate nucleation-related parameters. The distribution of induction times for each simulation, determined based on the calculated critical cluster size (n*), is shown in Figure 4.4.3-2. For simulations that did not successfully nucleate within 500 ns, the induction time was recorded as 500 ns. From Table 4.4.3-1, it can be observed that under our simulation conditions, the presence of methionine does not have a significant effect on promoting the hydrate nucleation rate and hydrate growth rate.

Additionally, we calculated the induction time and nucleation rate using Equation (3.4.4-1) [67] (based on the maximum likelihood estimate, MLE) and compared the results with those obtained from the MFPT method for both single-phase and two-phase

doi:10.6342/NTU202403841

systems, as shown in Table 4.4.3-2. From Table 4.4.3-2, it can be observed that all the induction times calculated using the MLE method are greater than the values obtained through the MFPT method, exhibiting a consistent trend. Moreover, as the sample size increases, the percent deviation decreases.

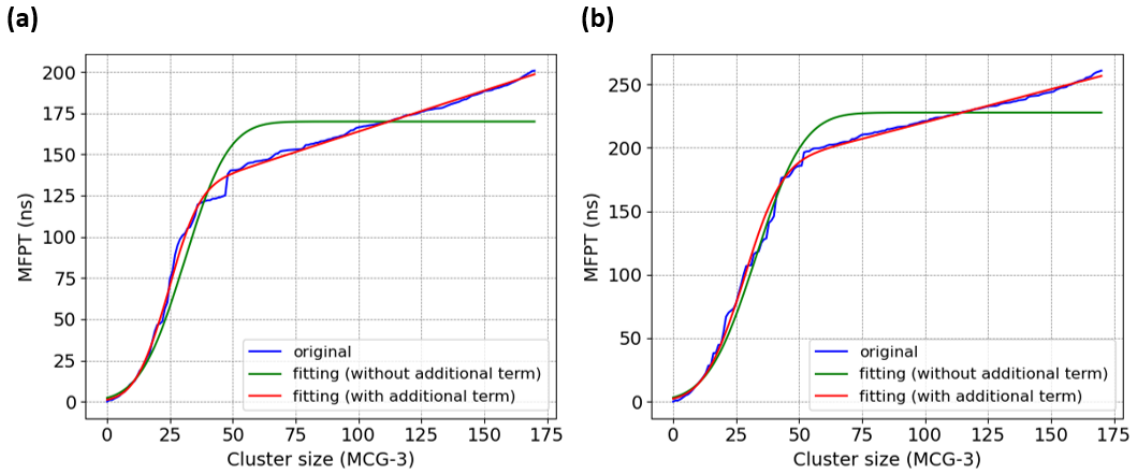

Figure 4.4.3-1 MFPT curve fitting results for CO_2 hydrate nucleation in two-phase systems at 262 K and 500 bar (20 sets of simulations for each system). (a) 0 Met system. (b) 1 Met system.

doi:10.6342/NTU202403841

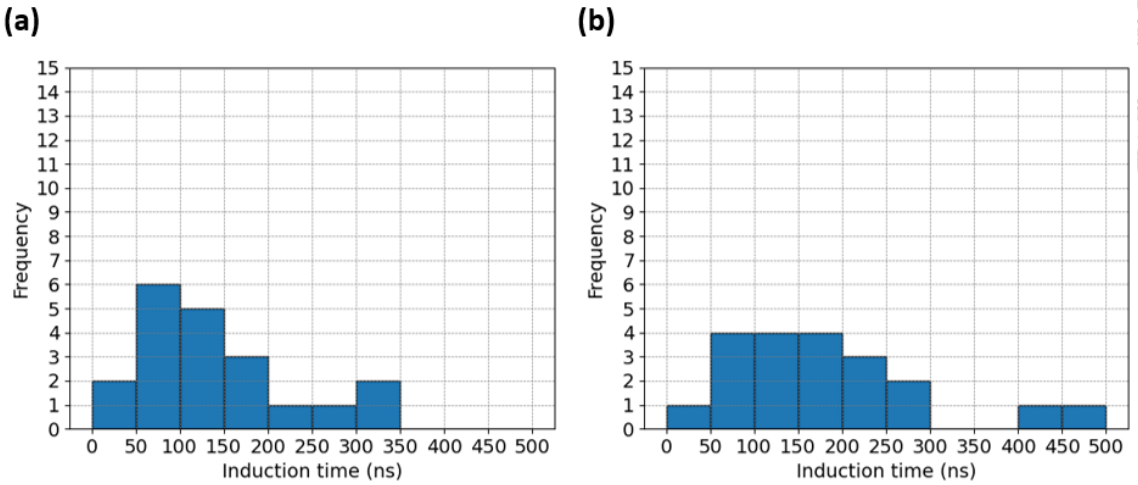

Figure 4.4.3-2 Distribution of induction time for CO_2 hydrate nucleation in two-phase systems at 262 K and 500 bar (20 sets of simulations for each system). (a) 0 Met system. (b) 1 Met system.

Table 4.4.3-1 MFPT curve fitting results for CO_2 hydrate nucleation in two-phase systems at 262 K and 500 bar. Each system has 20 simulation sets, and the values in parentheses are the standard errors.

System	τ_J (ns)	Z	n^* (MCG-3)	$J \times 10^5$ ($nm^{-3}ns^{-1}$)	G (MCG-3/ns)
0 Met	125.946 (0.785)	0.03983 (0.00043)	23.6 (0.2)	13.65642 (0.08515)	2.013 (0.033)
1 Met	182.184 (1.553)	0.03286 (0.00044)	27.3 (0.2)	9.44086 (0.08045)	1.920 (0.060)

doi:10.6342/NTU202403841

Table 4.4.3-2 Comparison of the induction time and nucleation rate calculated by mean first-passage time (MFPT) method and maximum likelihood estimate (MLE) method.

System	τ_J (ns)			J×10^5 ($nm^{-3}ns^{-1}$)		
	MFPT	MLE	Deviation (%)	MFPT	MLE	Deviation (%)
260 K, 30 bar (0 Met, 15 sets, single-phase)	94.34	125.17	32.68	25.940	19.552	-24.63
260 K, 30 bar (1 Met, 15 sets, single-phase)	117.23	137.58	17.36	20.756	17.685	-14.80
262 K, 30 bar (0 Met, 50 sets, single-phase)	284.41	309.67	8.88	8.605	7.903	-8.16
262 K, 30 bar (1 Met, 50 sets, single-phase)	343.40	356.59	3.84	7.085	6.823	-3.70
262 K, 500 bar (0 Met, 20 sets, two-phase)	125.95	139.26	10.57	13.656	12.351	-9.56
262 K, 500 bar (1 Met, 20 sets, two-phase)	182.18	191.05	4.87	9.441	9.003	-4.64

4.5 Effects of Methionine on CO_2 Hydrate Nucleation

4.5.1 Presence of Methionine around CO_2 Hydrate

Since we did not observe any promotional effect of methionine on the hydrate nucleation rate in the CO_2 hydrate nucleation tests, but did see an increase in the hydrate

doi:10.6342/NTU202403841

growth rate for systems with methionine compared to those without methionine in the single-phase system for CO_2 hydrate nucleation tests conducted at 262 K and 30 bar, we will focus on analyzing the possible reasons for the increase in hydrate growth rate caused by methionine.

We analyzed the moment of inertia of the largest hydrate cluster used to calculate the MCG-3 value to determine which side of the cluster grows faster and simultaneously analyzed the relative position of the methionine molecules to the cluster during its growth process. This allows us to understand how the presence of methionine affects the growth of the hydrate cluster. Specifically, we first moved the cluster's center of mass to the origin, and then obtained the moment of inertia tensor [82] of the cluster in the new three-dimensional Cartesian coordinate system, yielding the moments of inertia (eigenvalues) and the unit vectors of the three new coordinate axes (eigenvectors). By comparing the moment of inertia values of the three new coordinate axes, we can roughly determine the shape of the cluster, enabling us to quantitatively analyze the changes in cluster shape. The moment of inertia tensor in the three-dimensional Cartesian coordinate system is shown in Equation (4.5.1-1), where I_{xx} is $\sum_i m_i (y_i^2 + z_i^2)$, I_{yy} is $\sum_i m_i (x_i^2 + z_i^2)$, I_{zz} is $\sum_i m_i (x_i^2 + y_i^2)$, I_{xy} and I_{yx} are $-\sum_i m_i x_i y_i$, I_{xz} and I_{zx} are $-\sum_i m_i x_i z_i$, and I_{yz} and I_{zy} are $-\sum_i m_i y_i z_i$.

doi:10.6342/NTU202403841

$$\text{Moment of intertia tensor} = \begin{bmatrix} I_{xx} & I_{xy} & I_{xz} \\ I_{yx} & I_{yy} & I_{yz} \\ I_{zx} & I_{zx} & I_{zz} \end{bmatrix} \quad (4.5.1\text{-}1)$$

While calculating the cluster's moment of inertia, we also transformed the sulfur and nitrogen atoms of the methionine molecules from the original Cartesian coordinate system to the new Cartesian coordinate system using the unit vectors of three new axes obtained earlier. Since we moved the cluster's center of mass to the origin before calculating the moment of inertia, we also translated the sulfur and nitrogen atoms together with the carbon atoms of the CO_2 molecules nearest to them in the cluster before transforming them to new Cartesian coordinate system. This ensures that the relative positions of the cluster and methionine remain unchanged in the new Cartesian coordinate system, allowing us to more accurately assess the impact of methionine.

Figure 4.5.1-1 shows the moment of inertia calculation results from one selected simulation for each of the two systems. In this figure, the a-axis represents the axis with the smallest moment of inertia, and the c-axis represents the axis with the largest moment of inertia. The Figure 4.5.1-1 presents the results of the two smaller moments of inertia divided by the largest moment of inertia. A value of 0 indicates that no hydrate cluster is present at that time. From the results, it can be observed that both systems initially have two axes with larger moments of inertia and one axis with a smaller moment of inertia after nucleation. As the cluster grows, the differences in moments of inertia among the

doi:10.6342/NTU202403841

three axes rapidly decrease, indicating that the cluster shape evolves from an ellipsoid to a more spherical shape, regardless of the presence of methionine in the system. Figure 4.5.1-2 provides a schematic representation of this cluster growth behavior.

The current analysis of moments of inertia shows that the ratio Iaa/Icc increases rapidly during the period of fast hydrate growth. Since Iaa reflects the cluster growth on the plane formed by the b and c axes, and Icc reflects the cluster growth on the plane formed by the a and b axes, the ratio Iaa/Icc can represent the growth of the cluster in the BC-plane relative to the AB-plane. Therefore, we analyzed the successfully nucleated simulations from both systems, calculated the slopes of Iaa/Icc during the period from induction time to the point when the MCG-3 value reaches 120, and averaged the slopes. This analysis helps observe the relative growth rates of the clusters in the BC-plane compared to the AB-plane during hydrate growth. The observation cut-off at a MCG-3 value of 120 is consistent with the MFPT analysis in Section 4.4.2, which also considered the MFPT curve up to a MCG-3 value of 120 to analyze hydrate nucleation and growth rates. The calculated average slope of Iaa/Icc for the systems without methionine is 0.00438 (1/ns), while for the systems with methionine, it is 0.00504 (1/ns). The numbers of successfully nucleated simulations were 40 and 37 for the systems without and with methionine, respectively. This indicates that in the system with methionine, the cluster

doi:10.6342/NTU202403841

grows faster in the BC-plane relative to the AB-plane, causing the cluster shape to transition more rapidly from an ellipsoid to a sphere.

Additionally, after transforming the coordinates of methionine to the new Cartesian coordinate system, we also calculated the distances between the sulfur and nitrogen atoms of methionine and the three new axes. This allowed us to roughly determine which axis methionine was closer to. Our observations indicate that during the rapid growth of the hydrate, methionine mostly stayed near the b-axis and c-axis, and Figure 4.5.1-3 illustrates a schematic diagram of this behavior. Figure 4.5.1-4 shows the calculation results from a selected sample.

At the same time, we calculated the minimum distances between the sulfur and nitrogen atoms of methionine and the carbon atoms of CO_2 in the cluster. We observed that the sulfur and nitrogen atoms of methionine remained within a range of 0.4 to 1.2 nm from the cluster during the rapid growth time segment of the hydrate cluster, as shown in Figure 4.5.1-5. This indicates that methionine stays very close to the cluster during the hydrate growth process. Additionally, since we know that methionine tends to stay near the b-axis or c-axis, which are the faster-growing sides during this period, it can be inferred that methionine contributes to some extent to the rapid growth of the hydrate.

doi:10.6342/NTU202403841

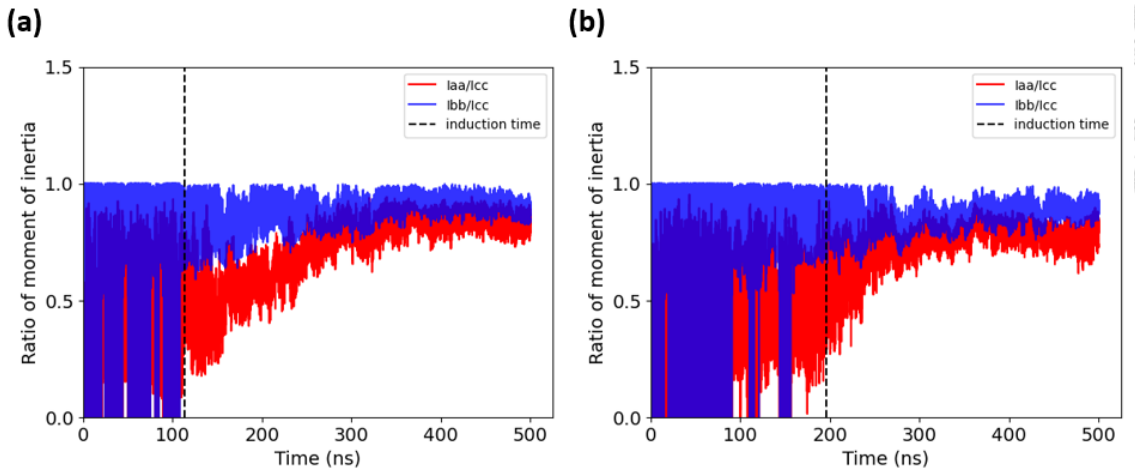

Figure 4.5.1-1 An example of moment of inertia for CO_2 hydrate nucleation in single-phase systems at 262 K and 30 bar. (a) 0 Met system. (b) 1 Met system.

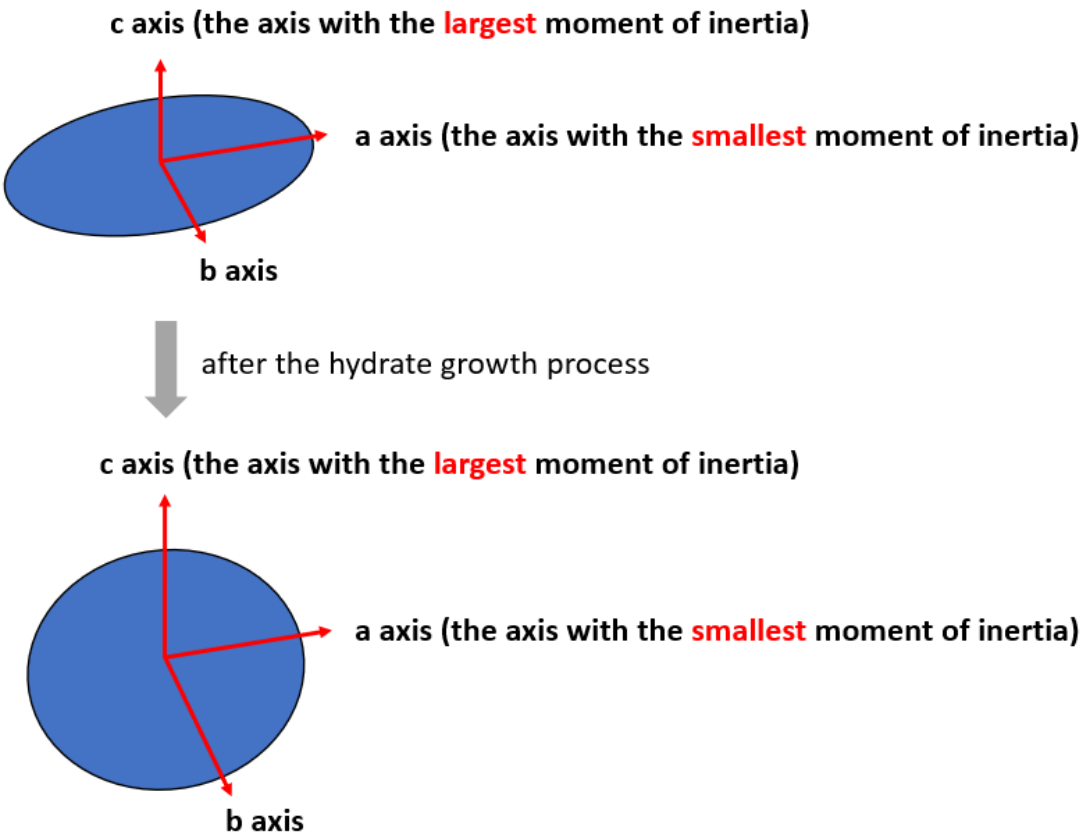

Figure 4.5.1-2 Schematic diagram for the variation of cluster shape.

doi:10.6342/NTU202403841

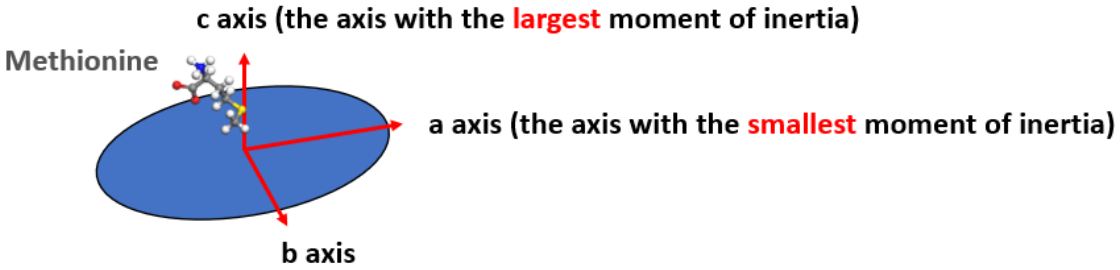

Figure 4.5.1-3 Schematic diagram of the relative position of methionine to the cluster during hydrate growth.

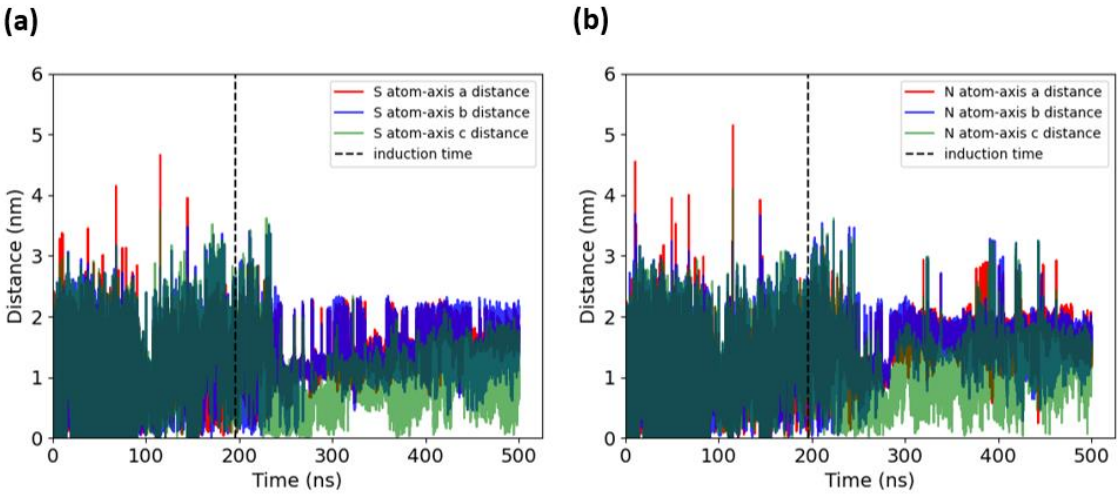

Figure 4.5.1-4 An example of distances between S and N atoms of methionine and new axes for CO_2 hydrate nucleation in single-phase systems at 262 K and 30 bar. (a) S atom. (b) N atom.

doi:10.6342/NTU202403841

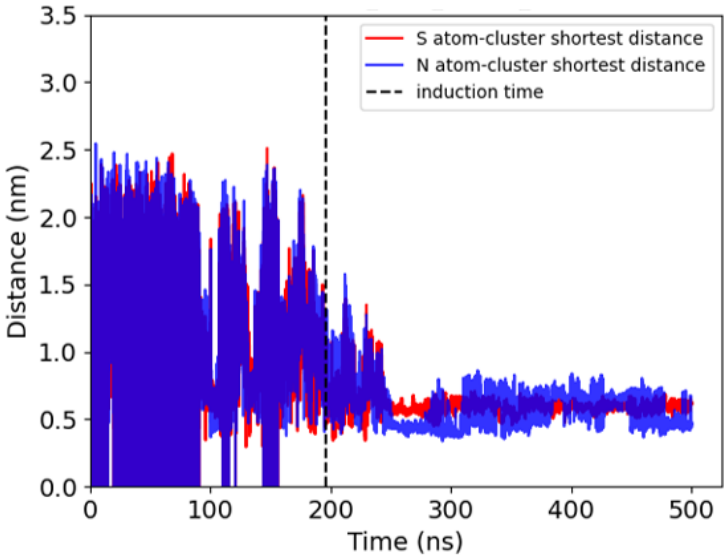

Figure 4.5.1-5 An example of shortest distances between S and N atoms of methionine and hydrate cluster for CO_2 hydrate nucleation in single-phase systems at 262 K and 30 bar.

doi:10.6342/NTU202403841

Chapter 5 Conclusions

In this study, MD simulations were conducted to explore the impact of different concentrations of methionine in the liquid phase on CO_2 hydrate growth and nucleation. From the simulation results of CO_2 hydrate growth, we found that when the concentration of methionine in the liquid phase of the initial system was 1 methionine molecule per 1472 water molecules (0.56 wt%), a slight promotion effect of methionine on CO_2 hydrate growth could be observed under conditions of 285 K and 30 bar. Upon analysis, we found that the addition of methionine barely affects the solubility of CO_2 in the liquid phase. Although it can slightly increase the diffusivity of CO_2 molecules in the liquid phase, this is accompanied by a slight decrease in the diffusivity of water molecules in the liquid phase. This synergistic effect may be one of the reasons we only observe the promotion effect in systems with relatively low methionine concentrations. Furthermore, during the hydrate growth process, we observed that methionine tends to stay near the hydrate-liquid interface rather than in the liquid phase, which could reduce its impact on the diffusivity of most CO_2 and water molecules in the liquid phase, leading to a weaker promotion effect in this aspect. Additionally, we found that when there is an average of approximately 0.4 sulfur atoms of methionine present within a 1.0 nm range from the hydrate-liquid interface throughout the simulation duration, a promotion effect on CO_2 hydrate growth

doi:10.6342/NTU202403841

can also be observed. The inability to observe the promotion effect when more methionine molecules present near the interface is likely due to methionine becoming trapped on the hydrate, thereby reducing the hydrate growth rate on that side. As the amount of methionine molecules around the hydrate-liquid interface increases, the likelihood of methionine getting trapped on the hydrate also increases.

From the simulation results of CO_2 hydrate nucleation, although we did not observe any promoting effect of methionine on CO_2 hydrate nucleation under our simulation conditions, we found that the hydrate growth rate after nucleation was increased by 36.61% in the system with a methionine concentration of 1 methionine molecule per 1000 water molecules (0.82 wt%) compared to the system without methionine under the conditions of 262 K and 30 bar in the single-phase CO_2 hydrate nucleation test (the subcooling temperature is about 26 K). This concentration is very close to the methionine concentration (0.56 wt%) observed to have a promoting effect in previous CO_2 hydrate growth tests, demonstrating consistency in the results. Additionally, we observed that methionine molecules tend to stay on the side of the hydrate that grows faster and stay very close to the hydrate during the hydrate growth process. Therefore, we can infer that methionine contributes to the rapid growth of the hydrate.

For the future research, further validation of the force field parameters for

doi:10.6342/NTU202403841

methionine molecules can be performed by comparing simulation results from different models. Additionally, conducting CO_2 hydrate growth test directly at 262 K and 30 bar could potentially reveal stronger promoting effects compared to the current conditions of 285 K and 30 bar.

doi:10.6342/NTU202403841

Reference

1. Sloan, E.D., *Fundamental principles and applications of natural gas hydrates.* Nature, 2003. **426**(6964): p. 353-359.
2. Sloan Jr, E.D. and C.A. Koh, *Clathrate hydrates of natural gases, 3rd*. 2007: CRC press.
3. Kvenvolden, K.A. and B.W. Rogers, *Gaia's breath—global methane exhalations.* Marine and Petroleum Geology, 2005. **22**(4): p. 579-590.
4. Sloan, E.D., *Clathrate hydrates: the other common solid water phase.* Industrial & Engineering Chemistry Research, 2000. **39**(9): p. 3123-3129.
5. Gornitz, V. and I. Fung, *Potential distribution of methane hydrates in the world's oceans.* Global Biogeochemical Cycles, 1994. **8**(3): p. 335-347.
6. Dickens, G.R., C.K. Paull, and P. Wallace, *Direct measurement of in situ methane quantities in a large gas-hydrate reservoir.* Nature, 1997. **385**(6615): p. 426-428.
7. Lee, S.-Y. and G.D. Holder, *Methane hydrates potential as a future energy source.* Fuel processing technology, 2001. **71**(1-3): p. 181-186.
8. Gbaruko, B., et al., *Gas hydrates and clathrates: Flow assurance, environmental and economic perspectives and the Nigerian liquified natural gas project.* Journal of Petroleum Science and Engineering, 2007. **56**(1-3): p. 192-198.
9. Gudmundsson, J.S., M. Parlaktuna, and A. Khokhar, *Storage of natural gas as frozen hydrate.* SPE Production & Facilities, 1994. 9(01): p. 69-73.
10. Zhang, Y., et al., *Solidified hydrogen storage (Solid-HyStore) via clathrate hydrates.* Chemical Engineering Journal, 2022. **431**: p. 133702.
11. Moon, S., et al., *Critical hydrogen concentration of hydrogen-natural gas blends in clathrate hydrates for blue hydrogen storage.* Renewable and Sustainable Energy Reviews, 2021. **141**: p. 110789.
12. Kim, D.-Y., Y. Park, and H. Lee, *Tuning clathrate hydrates: Application to hydrogen storage.* Catalysis today, 2007. **120**(3-4): p. 257-261.
13. Chapoy, A., R. Anderson, and B. Tohidi, *Low-pressure molecular hydrogen storage in semi-clathrate hydrates of quaternary ammonium compounds.* Journal of the American chemical society, 2007. **129**(4): p. 746-747.
14. Babu, P., et al., *A review of clathrate hydrate based desalination to strengthen energy–water nexus.* ACS Sustainable Chemistry & Engineering, 2018. **6**(7): p. 8093-8107.
15. He, T., et al., *A novel conceptual design of hydrate based desalination (HyDesal) process by utilizing LNG cold energy.* Applied energy, 2018. 222: p. 13-24.

doi:10.6342/NTU202403841

16. Bhattacharjee, G., et al., *Carbon dioxide sequestration: influence of porous media on hydrate formation kinetics.* ACS Sustainable Chemistry & Engineering, 2015. **3**(6): p. 1205-1214.
17. Cao, X., et al., *Hydrate-based CO2 sequestration technology: Feasibilities, mechanisms, influencing factors, and applications.* Journal of Petroleum Science and Engineering, 2022. 219: p. 111121.
18. Rehman, A.N., et al., *Research advances, maturation, and challenges of hydrate-based CO2 sequestration in porous media.* ACS Sustainable Chemistry & Engineering, 2021. **9**(45): p. 15075-15108.
19. Hammerschmidt, E., *Formation of gas hydrates in natural gas transmission lines.* Industrial & engineering chemistry, 1934. **26**(8): p. 851-855.
20. Bishnoi, P. and P.D. Dholabhai, *Equilibrium conditions for hydrate formation for a ternary mixture of methane, propane and carbon dioxide, and a natural gas mixture in the presence of electrolytes and methanol.* Fluid Phase Equilibria, 1999. **158**: p. 821-827.
21. Dholabhai, P.D., J.S. Parent, and P.R. Bishnoi, *Equilibrium conditions for hydrate formation from binary mixtures of methane and carbon dioxide in the presence of electrolytes, methanol and ethylene glycol.* Fluid Phase Equilibria, 1997. 141(1-2): p. 235-246.
22. Koh, C., et al., *Mechanisms of gas hydrate formation and inhibition.* Fluid Phase Equilibria, 2002. 194: p. 143-151.
23. Lopez, M.J. and S.S. Mohiuddin, *Biochemistry, essential amino acids*, in *StatPearls [Internet]*. 2023, StatPearls Publishing.
24. Willke, T., *Methionine production-a critical review.* Applied Microbiology and Biotechnology, 2014. **98**(24): p. 9893-9914.
25. Wu, G., *Functional amino acids in nutrition and health*. 2013, Springer. p. 407-411.
26. Majid, A.A., J. Worley, and C.A. Koh, *Thermodynamic and kinetic promoters for gas hydrate technological applications.* Energy & Fuels, 2021. **35**(23): p. 19288-19301.
27. Lee, Y.-J., et al., *Phase Equilibrium Studies of Tetrahydrofuran (Thf)+ Ch4, Thf+ Co2, Ch4+ Co2, and Thf+ Co2+ Ch4 Hydrates.* Journal of Chemical & Engineering Data, 2012. **57**(12): p. 3543-3548.
28. Seo, Y.-T., S.-P. Kang, and H. Lee, *Experimental determination and thermodynamic modeling of methane and nitrogen hydrates in the presence of THF, propylene oxide, 1, 4-dioxane and acetone.* Fluid Phase Equilibria, 2001. **189**(1-2): p. 99-110.
29. Herslund, P.J., et al., *Measuring and modelling of the combined thermodynamic*

doi:10.6342/NTU202403841

promoting effect of tetrahydrofuran and cyclopentane on carbon dioxide hydrates. Fluid Phase Equilibria, 2014. **381**: p. 20-27.
30. Sun, Z.-G., et al., *Gas hydrate phase equilibrium data of cyclohexane and cyclopentane.* Journal of Chemical & Engineering Data, 2002. **47**(2): p. 313-315.
31. Arjmandi, M., A. Chapoy, and B. Tohidi, *Equilibrium data of hydrogen, methane, nitrogen, carbon dioxide, and natural gas in semi-clathrate hydrates of tetrabutyl ammonium bromide.* Journal of chemical & engineering data, 2007. **52**(6): p. 2153-2158.
32. Sun, Z.-G. and L. Sun, *Equilibrium conditions of semi-clathrate hydrate dissociation for methane+ tetra-n-butyl ammonium bromide.* Journal of Chemical & Engineering Data, 2010. **55**(9): p. 3538-3541.
33. Molokitina, N.S., et al., *Carbon dioxide hydrate formation with SDS: Further insights into mechanism of gas hydrate growth in the presence of surfactant.* Fuel, 2019. **235**: p. 1400-1411.
34. Du, J., H. Li, and L. Wang, Effects of ionic surfactants on methane hydrate formation kinetics in a static system. Advanced Powder Technology, 2014. 25(4): p. 1227-1233.
35. Veluswamy, H.P., Q.W. Hong, and P. Linga, *Morphology study of methane hydrate formation and dissociation in the presence of amino acid.* Crystal Growth & Design, 2016. **16**(10): p. 5932-5945.
36. Khandelwal, H., et al., *Effect of l-tryptophan in promoting the kinetics of carbon dioxide hydrate formation.* Energy & Fuels, 2020. 35(1): p. 649-658.
37. Cai, Y., et al., *CO2 hydrate formation promoted by a natural amino acid l-methionine for possible application to CO2 capture and storage.* Energy Technology, 2017. 5(8): p. 1195-1199.
38. Zhang, Y.T., et al., *Enhanced CO2 hydrate formation via biopromoter coupled with initial stirring activation.* Fuel, 2022. **330**: p. 9.
39. Liu, X.J., et al., *Comparison of SDS and (L)-Methionine in promoting CO2 hydrate kinetics: Implication for hydrate-based CO2 storage.* Chemical Engineering Journal, 2022. **438**: p. 13.
40. Xu, H., et al., *Enhanced CO2 hydrate formation using hydrogen-rich stones, L-Methionine and SDS: Insights from kinetic and morphological studies.* Energy, 2024. 291: p. 130280.
41. Rogers, R.E., et al., *Catalysis of gas hydrates by biosurfactants in seawater-saturated sand/clay.* The Canadian Journal of Chemical Engineering, 2003. 81(5): p. 973-980.
42. Heydari, A. and K. Peyvandi, *Study of biosurfactant effects on methane recovery*

doi:10.6342/NTU202403841

from gas hydrate by CO2 replacement and depressurization. Fuel, 2020. 272: p. 117681.
43. Hockney, R.W. and J.W. Eastwood, *Computer simulation using particles*. 2021: crc Press.
44. Lennard-Jones, J.E., *Cohesion.* Proceedings of the Physical Society, 1931. **43**(5): p. 461.
45. Allen, M.P., Tildesley, D. J, *Computer Simulations of Liquids.* 1987: Oxford: Oxford Science Publications.
46. Toukmaji, A.Y. and J.A. Board, *Ewald summation techniques in perspective: A survey.* Computer Physics Communications, 1996. **95**(2-3): p. 73-92.
47. Gibbs, J.W., *Elementary principles in statistical mechanics: developed with especial reference to the rational foundations of thermodynamics*. 1902: C. Scribner's sons.
48. Kittel, C.H.K., *Thermal Physics, 2nd.* 1980, San Francisco: W.H. Freeman and Company. P 31.
49. Nosé, S., *A molecular dynamics method for simulations in the canonical ensemble.* Molecular physics, 1984. **52**(2): p. 255-268.
50. Hoover, W.G., *CANONICAL DYNAMICS - EQUILIBRIUM PHASE-SPACE DISTRIBUTIONS.* Physical Review A, 1985. **31**(3): p. 1695-1697.
51. Berendsen, H.J.C., et al., *MOLECULAR-DYNAMICS WITH COUPLING TO AN EXTERNAL BATH.* Journal of Chemical Physics, 1984. **81**(8): p. 3684-3690.
52. Parrinello, M. and A. Rahman, *POLYMORPHIC TRANSITIONS IN SINGLE-CRYSTALS - A NEW MOLECULAR-DYNAMICS METHOD.* Journal of Applied Physics, 1981. **52**(12): p. 7182-7190.
53. Module, F., *Material Studio 5.0.* Accelrys Inc., San Diego, CA, 2009.
54. Pronk, S., et al., *GROMACS 4.5: a high-throughput and highly parallel open source molecular simulation toolkit.* Bioinformatics, 2013. **29**(7): p. 845-854.
55. Takeuchi, F., et al., *Water proton configurations in structures I, II, and H clathrate hydrate unit cells.* The Journal of chemical physics, 2013. **138**(12).
56. Hernández, B., et al., *Side chain flexibility and protonation states of sulfur atom containing amino acids.* Physical Chemistry Chemical Physics, 2011. **13**(38): p. 17284-17294.
57. Haynes, W.M., *CRC handbook of chemistry and physics*. 2016: CRC press.
58. Abascal, J.L.F., et al., *A potential model for the study of ices and amorphous water:: TIP4P/Ice -: art. no. 234511.* Journal of Chemical Physics, 2005. **122**(23): p. 9.
59. Harris, J.G. and K.H. Yung, *CARBON DIOXIDES LIQUID-VAPOR COEXISTENCE CURVE AND CRITICAL PROPERTIES AS PREDICTED BY A SIMPLE*

doi:10.6342/NTU202403841

MOLECULAR-MODEL. Journal of Physical Chemistry, 1995. **99**(31): p. 12021-12024.

60. Jorgensen, W.L. and J. Tirado-Rives, *Potential energy functions for atomic-level simulations of water and organic and biomolecular systems.* Proceedings of the National Academy of Sciences of the United States of America, 2005. **102**(19): p. 6665-6670.
61. Dodda, L.S., et al., *1.14*CM1A-LBCC: Localized Bond-Charge Corrected CM1A Charges for Condensed-Phase Simulations.* Journal of Physical Chemistry B, 2017. **121**(15): p. 3864-3870.
62. Dodda, L.S., et al., *LigParGen web server: an automatic OPLS-AA parameter generator for organic ligands.* Nucleic Acids Research, 2017. **45**(W1): p. W331-W336.
63. Wang, P.-W., D.T. Wu, and S.-T. Lin, *Promotion mechanism for the growth of CO 2 hydrate with urea using molecular dynamics simulations.* Chemical Communications, 2021. **57**(43): p. 5330-5333.
64. Rodger, P., T. Forester, and W. Smith, *Simulations of the methane hydrate/methane gas interface near hydrate forming conditions.* Fluid phase equilibria, 1996. **116**(1-2): p. 326-332.
65. Barnes, B.C., et al., *Two-component order parameter for quantifying clathrate hydrate nucleation and growth.* Journal of Chemical Physics, 2014. **140**(16): p. 6.
66. Wedekind, J., R. Strey, and D. Reguera, *New method to analyze simulations of activated processes.* The Journal of chemical physics, 2007. **126**(13).
67. Yuhara, D., et al., *Nucleation rate analysis of methane hydrate from molecular dynamics simulations.* Faraday Discussions, 2015. **179**: p. 463-474.
68. Walsh, M.R., et al., *Methane hydrate nucleation rates from molecular dynamics simulations: Effects of aqueous methane concentration, interfacial curvature, and system size.* The Journal of Physical Chemistry C, 2011. **115**(43): p. 21241-21248.
69. Yi, P., C.R. Locker, and G.C. Rutledge, *Molecular dynamics simulation of homogeneous crystal nucleation in polyethylene.* Macromolecules, 2013. **46**(11): p. 4723-4733.
70. Duan, Z., et al., *An improved model for the calculation of CO2 solubility in aqueous solutions containing Na+, K+, Ca2+, Mg2+, Cl−, and SO42−.* Marine chemistry, 2006. **98**(2-4): p. 131-139.
71. Allen, M.P., Tildesley, D. J, *Computer Simulations of Liquids.* 1987: Oxford: Oxford Science Publications.
72. Nijsing, R., R. Hendriksz, and H. Kramers, *Absorption of CO2 in jets and falling*

doi:10.6342/NTU202403841

films of electrolyte solutions, with and without chemical reaction. Chemical Engineering Science, 1959. **10**(1-2): p. 88-104.
73. Bozzo, A.T., et al., *The properties of the hydrates of chlorine and carbon dioxide.* Desalination, 1975. **16**(3): p. 303-320.
74. Anderson, G.K., *Enthalpy of dissociation and hydration number of carbon dioxide hydrate from the Clapeyron equation.* The Journal of Chemical Thermodynamics, 2003. **35**(7): p. 1171-1183.
75. Diamond, L.W., *Stability of CO2 clathrate hydrate+ CO2 liquid+ CO2 vapour+ aqueous KCl-NaCl solutions: Experimental determination and application to salinity estimates of fluid inclusions*.* Geochimica et Cosmochimica Acta, 1992. **56**(1): p. 273-280.
76. Shell, M.S., *Thermodynamics and statistical mechanics: an integrated approach*. 2015: Cambridge University Press.
77. Lievois, J., et al., *Development of an automated, high pressure heat flux calorimeter and its application to measure the heat of dissociation and hydrate numbers of methane hydrate.* Fluid phase equilibria, 1990. **59**(1): p. 73-97.
78. Kumełan, J., A.l. Pérez-Salado Kamps, and G. Maurer, *Solubility of CO2 in aqueous solutions of methionine and in aqueous solutions of (K2CO3 and methionine).* Industrial & engineering chemistry research, 2010. **49**(8): p. 3910-3918.
79. Nighswander, J.A., N. Kalogerakis, and A.K. Mehrotra, *Solubilities of carbon dioxide in water and 1 wt.% sodium chloride solution at pressures up to 10 MPa and temperatures from 80 to 200. degree. C.* Journal of Chemical and Engineering Data, 1989. **34**(3): p. 355-360.
80. Kirkwood, J.G., *Molecular distribution in liquids.* Journal of Chemical Physics, 1939. **7**(10): p. 919-925.
81. Skripov, V.P. and A. Skripov, *Spinodal decomposition (phase transitions via unstable states).* Soviet Physics Uspekhi, 1979. **22**(6): p. 389.
82. Beatty, M.F. and M.F. Beatty, *The Moment of Inertia Tensor.* Principles of Engineering Mechanics: Volume 2 Dynamics—The Analysis of Motion, 2006: p. 355-404.

doi:10.6342/NTU202403841